Structural dynamics of supercooled water from quasielastic neutron scattering and molecular simulations

Johan Qvist, Helmut Schober, and Bertil Halle

Related Articles

Additional information on J. Chem. Phys.

Structural dynamics of supercooled water from quasielastic neutron scattering and molecular simulations

Johan Qvist,[1] Helmut Schober,[2] and Bertil Halle[1,a)]

[1]*Biophysical Chemistry, Lund University, POB 124, SE-22100 Lund, Sweden*
[2]*Institut Laue-Langevin, BP 156, F-38042 Grenoble Cedex 9, France*

One of the outstanding challenges presented by liquid water is to understand how molecules can move on a picosecond time scale despite being incorporated in a three-dimensional network of relatively strong H-bonds. This challenge is exacerbated in the supercooled state, where the dramatic slowing down of structural dynamics is reminiscent of the, equally poorly understood, generic behavior of liquids near the glass transition temperature. By probing single-molecule dynamics on a wide range of time and length scales, quasielastic neutron scattering (QENS) can potentially reveal the mechanistic details of water's structural dynamics, but because of interpretational ambiguities this potential has not been fully realized. To resolve these issues, we present here an extensive set of high-quality QENS data from water in the range 253–293 K and a corresponding set of molecular dynamics (MD) simulations to facilitate and validate the interpretation. Using a model-free approach, we analyze the QENS data in terms of two motional components. Based on the dynamical clustering observed in MD trajectories, we identify these components with two distinct types of structural dynamics: picosecond local (L) structural fluctuations within dynamical basins and slower interbasin jumps (J). The Q-dependence of the dominant QENS component, associated with J dynamics, can be quantitatively rationalized with a continuous-time random walk (CTRW) model with an apparent jump length that depends on low-order moments of the jump length and waiting time distributions. Using a simple coarse-graining algorithm to quantitatively identify dynamical basins, we map the Newtonian MD trajectory on a CTRW trajectory, from which the jump length and waiting time distributions are computed. The jump length distribution is Gaussian and the rms jump length increases from 1.5 to 1.9 Å as the temperature increases from 253 to 293 K. The rms basin radius increases from 0.71 to 0.75 Å over the same range. The waiting time distribution is exponential at all investigated temperatures, ruling out significant dynamical heterogeneity. However, a simulation at 238 K reveals a small but significant dynamical heterogeneity. The macroscopic diffusion coefficient deduced from the QENS data agrees quantitatively with NMR and tracer results. We compare our QENS analysis with existing approaches, arguing that the apparent dynamical heterogeneity implied by stretched exponential fitting functions results from the failure to distinguish intrabasin (L) from interbasin (J) structural dynamics. We propose that the apparent dynamical singularity at ∼220 K corresponds to freezing out of J dynamics, while the calorimetric glass transition corresponds to freezing out of L dynamics. © *2011 American Institute of Physics*. [doi:10.1063/1.3578472]

I. INTRODUCTION

Water owes its distinct physical properties to the disordered H-bond network that pervades the liquid.[1] Whereas the structure of bulk water under ambient conditions has been thoroughly characterized,[2] a microscopic understanding of water dynamics is only beginning to emerge. Time-resolved vibrational spectroscopy and molecular simulations have provided valuable insights about fast dynamics,[3–6] including the elementary step of H-bond switching,[7–9] but much less is known about the collective rearrangements of the H-bond network, referred to as structural dynamics, that govern water dynamics on longer time scales.[10]

Studies of water structural dynamics often extend into the supercooled regime,[11,12] where the local structure of the H-bond network gradually approaches the tetrahedral order of hexagonal ice while the structural dynamics are slowed down dramatically. The long-standing challenge presented by supercooled water is to understand the microscopic basis of the very strong temperature dependence of structural relaxation times and their apparent divergence at a singular temperature in the vicinity of 220 K, which is unattainable because homogeneous nucleation intervenes.[13,14]

At a phenomenological level, the behavior of water in this temperature range is reminiscent of, but less extreme than, the behavior of glass-forming liquids on approaching the dynamical glass transition.[15] Based on this (imperfect) analogy, concepts and theories developed with nonaqueous glass-forming systems in mind[15–21] have been applied to supercooled water.[22–26] However, the glass transition is

---

a)Author to whom correspondence should be addressed. Electronic mail: bertil.halle@bpc.lu.se.

far from understood even for systems as simple as a binary Lennard-Jones mixture, where structural relaxation is governed by short-range repulsion rather than, as in water, by a three-dimensional network of strong (compared to $k_B T$) H-bonds.

Molecular dynamics (MD) simulations can provide detailed information about supercooled water dynamics, but understanding in terms of simple concepts and models does not emerge automatically. Moreover, given that subtle structural changes have dramatic effects on dynamics, simulations using force fields benchmarked primarily against ambient thermodynamics and structure may not be quantitatively reliable in the supercooled regime. Accurate experimental data on structural relaxation in supercooled water are therefore of critical importance. Quasielastic incoherent neutron scattering (QENS) is perhaps the most powerful technique in this regard since it can probe single-particle dynamics on a broad range of length and time scales.[27–29] But while QENS data are potentially rich in information, there is currently no consensus on how to interpret QENS data from bulk water, let alone from more complex aqueous systems.

It was noted early on that the QENS peak is narrower at high momentum transfer, Q, than expected for continuous translational diffusion,[30,31] suggesting that molecular motion in liquid water occurs by finite jumps, as for defect-mediated diffusion in solids. While QENS data from water and aqueous solutions are still widely interpreted in terms of jump models developed half a century ago,[32,33] the disturbing fact is that these jumps have never been identified in MD simulations.

As the QENS technique was improved and measurements were extended into the supercooled regime, a second, broader spectral component was identified and attributed to molecular rotation.[34,35] The data could be rather well described by a model that attributes the observed proton dynamics to two independent molecular motions: continuous rotational diffusion superimposed on jumplike translation.[35] Since this model has been widely adopted in subsequent QENS studies of water[36] and aqueous solutions,[37,38] we refer to it as the standard model. The popularity of this model derives largely from its ability to rationalize extensive sets of QENS data in terms of a small number of parameters. However, even its originators cautioned that the assumptions underlying the model may not be valid.[35]

Ominously, the rotational correlation time deduced from standard-model analysis of QENS data is significantly smaller and has a much weaker temperature dependence than that obtained more directly from nuclear spin relaxation rates.[39] It has been argued[40] that this discrepancy, at least above room temperature, can be partly attributed to the standard model's description of water rotation as a small-step diffusion process, whereas MD simulations[8,41] and vibrational spectroscopy[9] show that water molecules reorient mainly through large-angle jumps. But other MD simulations indicate that the small rotational contribution to the QENS spectrum is largely cancelled by a rotation–translation cross term,[42,43] implying that QENS data provide little or no information about water rotation. What is then the origin of the broad component of the QENS spectrum?

Furthermore, at low temperatures and high Q, the width of the narrow (translational) component determined with the standard model[35] deviates strongly from the continuous-diffusion limit, DQ^2; whereas, in simulations, this deviation is much less pronounced.[42,43] This discrepancy, as well as the inferred strong increase of the jump length on cooling,[35] casts further doubt on the validity of the standard model.

An alternative approach for interpreting QENS data, known as the relaxing cage model (RCM), has been proposed.[44,45] The RCM was apparently inspired by the finding that structural relaxation in many glass-forming liquids is nonexponential and can be fitted with the empirical stretched exponential (Kohlrausch) function, $\exp[-(\tau/\tau_K)^\beta]$.[15,18–20] The exponential translational and rotational relaxation functions appearing in the standard model are thus replaced by stretched exponentials in the RCM. The RCM has been used to interpret QENS data from bulk water (at elevated pressure),[46,47] nanoconfined water,[48] and aqueous solutions.[49,50] Given that the structural relaxation time, τ_K, and the stretching exponent, β, (and their rotational counterparts in some versions of the RCM) are allowed to vary (empirically) with Q, it is perhaps not surprising that the RCM can be well fitted to QENS data. Unfortunately, it is difficult to test the RCM since the *ad hoc* replacement of exponentials with stretched exponentials introduces operational parameters that cannot be rigorously related to independent dynamical and structural data. Furthermore, some applications of the RCM retain the questionable rotation–translation decoupling approximation and the (rotational) elastic incoherent structure factor (EISF) that follows from it.[51]

To resolve these interpretational issues, we have collected an extensive set of QENS data in the temperature range 253–293 K, benefiting from improvements in neutron spectrometer performance since the classic study of Teixeira *et al.*[35] and using a sample geometry that minimizes multiple scattering.[52] To analyze these data, we first use a model-free approach where the widths of the two Lorentzians are determined without constraining their relative amplitudes. For the subsequent interpretation of the width, Γ_1, of the narrow Lorentzian, we use a continuous-time random walk (CTRW) model that, under rather general conditions, predicts the same functional dependence of Γ_1 on Q as the classical model.[32,33,35] The macroscopic diffusion coefficient deduced in this way agrees quantitatively with NMR and tracer results.[53,54] The second parameter in the CTRW model is an *apparent* jump length, determined by low-order moments of the waiting time and jump length distributions.

Our new interpretational approach is validated by MD simulations at the experimental temperatures. Furthermore, we show that the MD trajectory can be mapped on a continuous-time random walk. We thus identify the jumps, responsible for the nonclassical Q-dependence of Γ_1, as transitions between *dynamical* basins. In this picture, the broad component of the QENS spectrum is attributed to intrabasin dynamics on the 1–5 ps time scale, thus explaining why the associated EISF (the relative weight of the narrow component) deviates strongly from previous models. Furthermore, the magnitude and temperature dependence of the apparent jump length deduced from the QENS data are quantita-

tively consistent with the waiting time and jump length distributions computed from the MD-derived CTRW trajectories. In the temperature range of our QENS measurements ($\geq$253 K), the waiting time distribution is exponential, consistent with the observed Lorentzian shape of the narrow QENS component. But a clear deviation from Poisson statistics, indicative of dynamical heterogeneity, is revealed by the MD simulation at 238 K.

II. METHODS

A. QENS experiment

To reduce the probability of heterogeneous ice nucleation during the QENS measurements, ultrapure H_2O (TraceSelect-Ultra, Fluka) was passed through a 20-nm filter (Anatope 10+, Whatman) and was then transferred to 0.3/0.4 mm ID/OD quartz capillaries (CV3040Q, VitroCom). The flame-sealed capillaries were tested for supercooling and discarded if freezing occurred within 72 h at 253 K. To minimize multiple scattering,[28] the capillaries were distributed along the perimeter of a 20 mm diameter circle in two groups of 10 capillaries confined to circular arc segments ~15 mm in width perpendicular to the neutron beam. To eliminate scattering from the sample holder, all exposed aluminum surfaces were cadmium plated, leaving a capillary length of 52 mm exposed to the 15×50 mm^2 neutron beam. The sample holder, placed in an ILL Orange cryostat that regulated the sample temperature to within 0.1 K, was optically aligned to bring the two groups of capillaries into a staggered configuration with respect to the neutron beam.

The QENS measurements were performed at the cold neutron time-of-flight spectrometer IN5 at Institut Laue-Langevin (http://www.ill.eu/instruments-support/instruments-groups/instruments/in5/).[55] Data were collected at six temperatures from 252.9 to 293.4 K (Table III). The master chopper frequency was 12 000 rpm and the frame overlap chopper frequency was set to 8000, 9600, and 10 285 rpm for incident neutron wavelengths, λ_0, of 5, 8, and 12 Å, respectively. The momentum transfer window used for analysis extended from 0.15 Å^{-1} (at the three lowest temperatures) or 0.40 Å^{-1} (at the three highest temperatures) up to 2.15 Å^{-1} with a spatial resolution better than 0.01 Å^{-1}.[55] Acquisition times were 4 h (at 5 and 12 Å) or 6 h (at 8 Å) using 512 (at 5 and 8 Å), or 1024 (at 12 Å) time-of-flight channels. The total neutron count on the detector array was 9×10^7 at $\lambda_0 = 5$ Å. No freezing was detected during any of these runs. (During a 4 h run at 250 K, one of the 20 capillaries froze. These data were therefore discarded.) Apart from the sample runs, QENS data were recorded at each wavelength and at a single temperature of 272.9 K from the sample holder with empty capillaries, from the cryostat without sample holder and from a cylindrical vanadium foil in place of the sample holder.

B. QENS data reduction

Data reduction was performed with the large array manipulation program, (LAMP) (http://www.ill.fr/data_treat/lamp/lamp.html). The primary data reduction protocol included correction for variable sample–detector distance, normalization with respect to incident neutron flux, and assignment of scattering angles. In the first step of the secondary data reduction protocol, background scattering was removed by subtracting the intensity from empty capillaries after multiplying it by an empirically determined effective sample transmission factor of 0.86 for the three lowest temperatures. (For the three highest temperatures, where the sample holder had a slightly different position in the cryostat, a transmission factor of 0.80 was used.) Using the empty-cryostat data, a similar subtraction was performed on the vanadium data (with an effective transmission factor of 0.60). Next, the sample scattering data were corrected for the variation of detector efficiency with scattering angle (using the elastic vanadium scattering data) and with neutron energy transfer. The neutron counts in the 512 or 1024 time-of-flight channels were then converted to neutron intensity, $I(\phi, \omega)$, as a function of neutron energy transfer, $\hbar\omega$, with a negative energy transfer corresponding to neutron energy gain ("up-scattering") or sample energy loss. Finally, the scattering angle, ϕ, was converted to momentum transfer, $\hbar Q$, using a Q bin width of 0.05 Å^{-1}. The scattering intensity matrix, $I(Q, \omega)$, thus obtained was analyzed without any correction for multiple scattering. Considering that the mean free path of a 5 Å neutron in H_2O (1.7 mm) is an order of magnitude larger than the capillary radius, we expect the dominant (narrow) Lorentzian component of the neutron spectrum to be virtually unaffected by multiple scattering.

C. QENS data analysis

Neutron scattering from H_2O is essentially incoherent so the scattered intensity, $I(Q, \omega; \lambda_0)$, can be expressed as a convolution of the incoherent dynamic structure factor (DSF), $S(Q, \omega)$, and the resolution function, $\mathcal{R}(Q, \omega; \lambda_0)$:[27–29]

$$I(Q, \omega; \lambda_0) = \alpha(\lambda_0)\, S(Q, \omega) \otimes \mathcal{R}(Q, \omega; \lambda_0). \quad (2.1)$$

For the IN5 spectrometer, the resolution function is well approximated by a Gaussian,

$$\mathcal{R}(Q, \omega; \lambda_0) = \frac{1}{\sqrt{2\pi}\,\sigma(Q; \lambda_0)}\, \exp\left(-\frac{\omega^2}{2\,[\sigma(Q; \lambda_0)]^2}\right) \quad (2.2)$$

The FWHM energy resolution,

$$R(Q; \lambda_0) = \sqrt{8\ln 2}\,\sigma(Q; \lambda_0), \quad (2.3)$$

was determined by fitting Eq. (2.2) to the vanadium spectra (Fig. 1). Although the wings are somewhat less intense, the main part of the vanadium spectrum is very nearly Gaussian. To determine the resolution as accurately as possible, we only included data above 15% of maximum amplitude in the fit. At small Q, the resolution is ~84, 22, and 6.5 μeV at $\lambda_0 = 5$, 8, and 12 Å, respectively (Fig. 2).

In the quasielastic regime, defined here as $|\hbar\omega| \leq 2.5$ meV, all our spectra can be accurately represented as a convolution of the Gaussian resolution function in Eq. (2.2) and a DSF consisting of two Lorentzians plus a constant ("inelastic") term. The model-free fitting function used for all
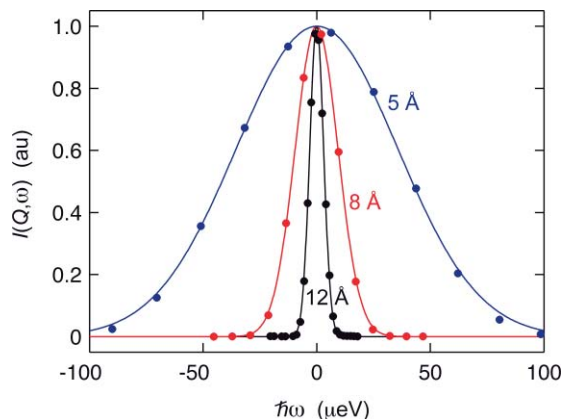
FIG. 1. Normalized vanadium spectra at $Q = 0.5$ Å^{-1} and $\lambda_0 = 5$, 8, and 12 Å. The curves are Gaussian fits to data points above 15% of maximum amplitude according to Eq. (2.2).

spectra was thus of the form,

$$I(Q, \omega; \lambda_0) = C(Q; \lambda_0)\{A(Q)\,\mathcal{V}_1(Q, \omega; \lambda_0) + [1 - A(Q)]$$
$$\times \mathcal{V}_2(Q, \omega; \lambda_0)\} + B(Q; \lambda_0), \qquad (2.4)$$

with the normalization constraint $0 \leq |A(Q)| \leq 1$ implemented by writing $A(Q) = \cos^2 \theta(Q)$. The Voigt function, $\mathcal{V}_n(Q, \omega; \lambda_0)$, is the convolution of the Gaussian resolution function in Eq. (2.2) and a normalized Lorentzian function with HWHM linewidth Γ_n,

$$\mathcal{L}_n(Q, \omega) = \frac{1}{\pi} \frac{\Gamma_n(Q)}{[\Gamma_n(Q)]^2 + \omega^2}. \qquad (2.5)$$

The result of this convolution can be expressed as

$$\mathcal{V}_n(Q, \omega; \lambda_0) \equiv \mathcal{L}_n(Q, \omega) \otimes \mathcal{R}(Q, \omega; \lambda_0)$$
$$= \frac{1}{\sqrt{2\pi}\,\sigma(Q; \lambda_0)} \Re\left[\exp\left(-Z_n^2\right) \operatorname{erfc}(-i\,Z_n)\right], \qquad (2.6)$$

where $Z_n \equiv (\omega + i\,\Gamma_n)/(\sqrt{2}\,\sigma)$. The Faddeeva function within square brackets was evaluated numerically with the FFT algorithm.[56]
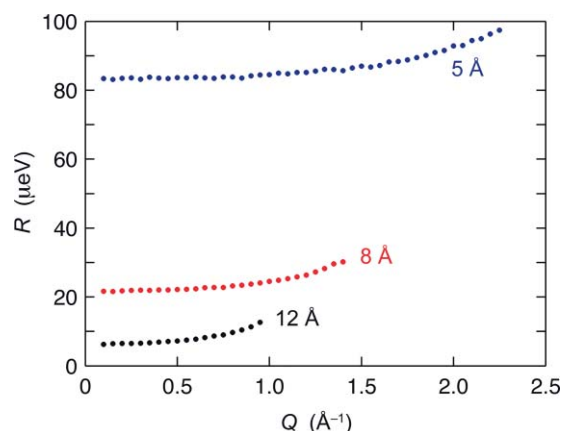

FIG. 2. Q-dependent energy resolution at $\lambda_0 = 5$, 8, and 12 Å, determined from Gaussian fits as in Fig. 1.

At the three lowest (highest) temperatures, 41 (36) spectra in the Q range 0.15 (0.40)–2.15 Å^{-1} were used to determine the Q-dependent parameters A, B, C, Γ_1, and Γ_2, with the two DSF components labeled such that $\Gamma_1 < \Gamma_2$. Our first priority here was to determine the width, Γ_1, of the narrow Lorentzian as accurately as possible. The frequency window used for the fits varied with Q and λ_0 such that $-\min(\hbar\,\omega_{\max}, 2.5\,\mathrm{meV}) \leq \hbar\omega \leq \min(\hbar\,\omega_{\max}, 0.4\,\mathrm{meV})$, with $\hbar\,\omega_{\max} = 10\,[\Gamma_1(Q) + R(Q; \lambda_0)]$. The Γ_1 values obtained from the fits turned out to be highly robust, with very little dependence on the choice of frequency window or on the number of Lorentzian components in the empirical fit function. All fits were performed with the Levenberg–Marquardt nonlinear least-squares algorithm.

D. MD simulation protocol

Classical molecular dynamics (MD) simulations were performed with GROMACS 4.0.3 (Ref. 57) for a system of 2048 water molecules in a cubic box with periodic boundary conditions. The integration time step, dt, was 1 fs and the neighbor list was updated after every step. Forces were computed with the SPCE effective pair potential.[58] A cutoff of 16 Å was used for both Lennard-Jones and Coulomb interactions and the long-range part of the latter was computed with particle-mesh Ewald summation using fourth-order interpolation and an FFT grid spacing of 0.11.

Simulations were performed over a 60 K temperature interval, including the six temperatures of the QENS experiments (see Sec. II A) and one lower temperature (Table I). The edge length, L, of the cubic simulation box was adjusted to reproduce the experimental density[59] (Table I) at the corresponding QENS temperature (or at 238 K). Although the QENS measurements were carried out at constant T and p, the simulations were performed in the microcanonical (NVE) ensemble without temperature or pressure coupling, which might perturb the dynamics. In the NpT ensemble, the relative rms density fluctuation for a 2048-molecule system would be ∼0.5%.[60] This fluctuation, which is suppressed in the NVE simulation, corresponds to ∼1% relative fluctuation in viscosity (and other structural dynamics observables), which is negligible compared to the order-of-magnitude variation in rate parameters over the temperature interval examined here. The drifts in total energy (<5 ppm ns^{-1}) and temperature (<0.03 K ns^{-1}), due to force truncation and numerical errors, were negligibly small. As expected,[60] the rms

TABLE I. Characteristics of MD simulations.

T (K)	σ_T (K)	E_{tot} (kJ mol^{-1})	ρ (g cm^{-3})	L (Å)
230.75	2.52	−45.604	0.9756	39.748
246.54	2.70	−44.022	0.9935	39.508
253.35	2.76	−43.376	0.9963	39.471
259.28	2.82	−42.808	0.9982	39.446
266.08	2.90	−42.197	0.9998	39.425
276.03	2.99	−41.291	0.9997	39.426
290.29	3.12	−40.039	0.9982	39.446

TABLE II. Effective temperature of MD simulations.[a]

T (K)	D_{MSD}[b] (10^{-10} m^2 s^{-1})	τ_R (ps)	T_D (K)	T_R (K)	T_{eff} (K)	$T_{eff} - T$ (K)
230.8	1.65(1)	32.7(3)	237.4	238.5	237.9	7.2
246.5	5.09(4)	9.47(4)	254.7	253.1	253.9	7.3
253.4	7.05(6)	6.67(2)	261.7	259.2	260.4	7.1
259.3	9.09(7)	5.02(2)	267.9	265.1	266.5	7.2
266.1	12.0(1)	3.87(3)	275.6	271.4	273.5	7.4
276.0	15.8(2)	2.72(1)	284.3	281.3	282.8	6.8
290.3	23.4(2)	1.82(1)	298.9	295.2	297.1	6.8

[a]Numbers within parentheses are estimated errors in the last digit.
[b]Corrected for the finite size of the simulation box according to Eq. (2.7).

temperature fluctuation (Table I) due to the finite system size was ~15% smaller than predicted for the NVT ensemble.

The SPCE water model is known to yield slightly too fast dynamics.[61] When comparing simulation with experiment, we compensate for this deficiency by replacing the nominal simulation temperature, T, determined from the mean kinetic energy, by an effective temperature, T_{eff}, defined as the arithmetic mean of the temperature, T_D, where the simulated diffusion coefficient, D_{MSD}, agrees with the experimental one, and the temperature, T_R, where the simulated ^{17}O rotational correlation time, τ_R, agrees with the experimental one. To this end, we use the power-law representations, Eqs. (2.8) and (2.13), of the experimental D and τ_R. As seen from Table II, T_{eff} is ~7 K higher than T in our temperature range.

E. MD trajectory analysis

Analysis using in-house MATLAB code was based, at each temperature, on 2048 fully equilibrated single-molecule trajectories of length 5 ns (at the three highest temperatures) or 10 ns (at the four lowest temperatures) and with coordinates saved every 5 fs up to 100 ps and every 100 fs thereafter.

The macroscopic translational diffusion coefficient, $D_{MSD}(L)$, was determined from a linear fit to the mean-square displacement (MSD), $\langle |\mathbf{R}(t + \tau) - \mathbf{R}(t)|^2 \rangle$, of the molecular center-of-mass (COM) in the τ interval 100–500 ps. This diffusion coefficient was then corrected for the hydrodynamic self-interaction induced by periodic boundary conditions on a

TABLE III. Results of fits to Q-dependent QENS parameters.[a]

T (K)	D_{NMR}[b] (10^{-10} m^2 s^{-1})	D_{QENS}[c] (10^{-10} m^2 s^{-1})	d[c] (Å)	u_{rms} (Å)
252.9	4.64	4.43(2)	0.839(3)	0.56(1)
257.8	5.92	5.85(2)	0.833(3)	0.55(1)
262.7	7.37	7.42(3)	0.800(3)	0.54(1)
272.7	10.8	11.01(4)	0.757(3)	0.58(1)
283.0	15.2	15.35(6)	0.745(3)	0.58(1)
293.4	20.4	20.19(7)	0.731(4)	0.60(1)

[a]Numbers within parentheses are estimated errors in the last digit.
[b]From Eq. (2.8).
[c]From fit with Eq. (3.2).

finite simulation box according to[62]

$$D_{MSD} = D_{MSD}(L) + \frac{\xi k_B T}{6 \pi \eta(T) L}, \qquad (2.7)$$

where $\xi = 2.837297$ and η is the experimental bulk water viscosity.[63] The results are given in Table II, with the standard error computed by subdividing the trajectory into 10 or 20 nonoverlapping 500 ps segments. (The uncorrected values are included in Table IV.) In the temperature range considered here, the experimental diffusion coefficient, D_{NMR}, obtained from NMR pulsed gradient spin echo (PGSE) (Ref. 53) or tracer[54] measurements, can be accurately represented by the power-law expression,

$$D_{NMR}/10^{-10}\,\text{m}^2\,\text{s}^{-1} = 159 \left(\frac{T/\text{K}}{212.6} - 1 \right)^{2.125}. \qquad (2.8)$$

The integral rotational correlation time, τ_R, which can be determined experimentally from the ^{17}O spin relaxation rate,[64,65] was computed as

$$\tau_R = \int_0^\infty d\tau\, \tilde{C}(\tau), \qquad (2.9)$$

where $\tilde{C}(\tau) = C(\tau)/C(0)$ and the electric field gradient (EFG) time correlation function (TCF) is given by

$$C(\tau) = \tfrac{1}{5} \langle \text{Tr}\{\mathsf{V}(0)\,\mathsf{V}(\tau)\} \rangle. \qquad (2.10)$$

Evaluating the trace in terms of the Cartesian components of the EFG tensor, V, we can express the reduced TCF as

$$\begin{aligned}
\tilde{C}(\tau) = \frac{1}{6}\left(1 + \frac{\eta^2}{3}\right)^{-1} & \langle M_{11}(0)\,M_{11}(\tau) + M_{22}(0)\,M_{22}(\tau) \\
& + M_{33}(0)\,M_{33}(\tau) + 2[M_{12}(0)\,M_{12}(\tau) \\
& + M_{13}(0)\,M_{13}(\tau) + M_{23}(0)\,M_{23}(\tau)]\rangle,
\end{aligned} \qquad (2.11)$$

where $\eta = 0.86$ is the asymmetry parameter of the ^{17}O EFG tensor[66] and

$$M_{ij} = (1 - \eta)e_x(i)e_x(j) + (1 + \eta)e_y(i)e_y(j) - 2e_z(i)e_z(j), \qquad (2.12)$$

where, for example, $e_x(i)$ is the i:th Cartesian laboratory-frame component of the unit vector along the x axis of the molecule-fixed principal EFG frame. To evaluate the integral in Eq. (2.9), the TCF was computed up to $\tau = 25, 50, 100$, or 200 ps and then exponentially extrapolated to $\tau \to \infty$. The results are given in Table II. In the temperature range considered here, the experimental ^{17}O integral rotational correlation time (Qvist, unpublished results), can be accurately represented by the power-law expression,

$$\tau_R/\text{ps} = 0.2203 \left(\frac{T/\text{K}}{223.2} - 1 \right)^{-1.866}. \qquad (2.13)$$

For a classical isotropic fluid, the self-part of the intermediate scattering function (ISF) can be expressed as[27–29]

$$F(Q, \tau) = \langle \cos\{\boldsymbol{Q} \cdot [\mathbf{R}(t + \tau) - \mathbf{R}(t)]\} \rangle, \qquad (2.14)$$

where $\mathbf{R}$ is the position of a given molecular site. The ISF was computed as the average of the 3 ISFs with $\boldsymbol{Q}$ along the

TABLE IV. Results of CTRW analysis of MD data.

T_{eff} (K)	ρ_{rms} (Å)	μ	δ	d^a (Å)	R_{basin} (Å)	τ_w (ps)	$\langle \cos \alpha \rangle$	D_{ES}^b $(10^{-10}$ m^2 s$^{-1})$	$D_{MSD}(L)^c$ $(10^{-10}$ m^2 s$^{-1})$
237.9	1.43	0.475	0.054	1.04	0.673	19.2	−0.021	1.70	1.65
253.9	1.54	0.472	−0.156	0.86	0.714	8.25	0.019	4.97	4.90
260.4	1.58	0.472	−0.196	0.83	0.725	6.50	0.023	6.74	6.74
266.5	1.63	0.474	−0.223	0.82	0.732	5.40	0.026	8.66	8.66
273.5	1.68	0.477	−0.246	0.81	0.738	4.55	0.029	11.0	11.4
282.8	1.76	0.484	−0.272	0.81	0.745	3.69	0.033	15.0	14.9
297.1	1.87	0.498	−0.296	0.84	0.749	2.94	0.040	21.6	22.0

[a]Computed with the aid of Eq. (3.20).
[b]Computed with the aid of Eq. (3.25).
[c]From mean-square displacement, uncorrected for the finite simulation box.

laboratory-fixed X, Y, and Z axes, each of which was averaged over time origins, t, and over all 2048 water molecules (or 4096 H atoms) in the simulation box. The periodic boundary conditions require the X, Y, and Z components of the Q vector to be integral multiples of $Q_{min} = 2\pi/L \approx 0.159$ Å^{-1}. For $\tau > 0.5$ ps, the ISF can be accurately represented by the biexponential function,

$$F(Q, \tau) = C^*(Q)\{A(Q) \exp[-\tau/\tau_1(Q)] + [1 - A(Q)] \exp[-\tau/\tau_2(Q)]\}, \quad (2.15)$$

the four parameters of which were determined from a Levenberg–Marquardt fit.

The DSF was computed from the MD-derived ISF as

$$S(Q, \omega) = \frac{1}{\pi} \int_0^\infty d\tau \, \cos(\omega\tau) \, F(Q, \tau), \quad (2.16)$$

with the ISF split in two parts as in Eq. (3.3). The Fourier transform of $F_V(Q, \tau)$ was computed by Filon quadrature[60] after appending an exponential tail for $\tau > 0.5$ ps, whereas the Fourier transform of the biexponential $F_S(Q, \tau)$ was computed analytically.

F. Random walk analysis

To map a Newtonian single-molecule MD trajectory on a random walk, we compute the running average position of the molecular center-of-mass, $\bar{\mathbf{R}}(n)$, from the positions, $\mathbf{R}(m)$, $m = 1 - n$, of that site in n consecutive MD time frames. This is done iteratively as

$$\bar{\mathbf{R}}(n) = \frac{(n-1)\bar{\mathbf{R}}(n-1) + \mathbf{R}(n)}{n}. \quad (2.17)$$

The average is further updated only if $\mathbf{R}(n + 1)$ remains within a prescribed distance, D_{max}, of the current average, that is, if

$$|\mathbf{R}(n + 1) - \bar{\mathbf{R}}(n)| \le D_{max}. \quad (2.18)$$

Otherwise, the n time frames are identified as a dynamical basin centered at $\bar{\mathbf{R}}(n)$ and the counter n is reset to 1 for the next basin. As a measure of the size of the basin, we use the rms radius of gyration,

$$R_{basin} = \left\langle \frac{1}{n} \sum_{m=1}^{n} |\mathbf{R}(m) - \bar{\mathbf{R}}(n)|^2 \right\rangle^{1/2}, \quad (2.19)$$

where the angular brackets signify averaging over all basins.

Provided that D_{max} is chosen in a suitable range, this algorithm successfully identifies the dynamical basins in the Newtonian trajectory. For the calculations reported here, we used $D_{max} = 1.5$ Å. However, a strict implementation of this constraint will identify some basins that are very close to the immediately preceding basin. Physical considerations suggest that such strongly overlapping basins should be regarded as a single basin. Consequently, we merge consecutive basins if their centers are separated by less than a minimum jump length, ρ_{min}. For such merged basins, excursions exceeding D_{max} are thus permitted. We used $\rho_{min} = 0.7$ Å, but reasonable variations of this value produced only minor variations in the results. Qualitatively, a larger ρ_{min} yields fewer basins and slightly longer but less frequent basin-to-basin jumps. For example, increasing ρ_{min} from 0 (no mergers) to 0.7 Å in the 254 K simulation reduces the number of basins by 10%, thereby increasing the rms jump length by 5% while increasing the mean waiting time by 12%.

This dynamical coarse-graining algorithm produces time series of basin positions, $\bar{\mathbf{R}}_k$, and absolute jump times, t_k, from which we compute jump vectors $\boldsymbol{\rho}_k = \bar{\mathbf{R}}_{k+1} - \bar{\mathbf{R}}_k$, waiting times $\tau'_k = t_{k+1} - t_k$, and jump angles $\cos\alpha_k = (\boldsymbol{\rho}_{k+1} \cdot \boldsymbol{\rho}_k)/(\rho_{k+1}\rho_k)$. Distribution functions and their moments are then calculated from the $(1-4) \times 10^6$ basins (depending on temperature) generated from the 2048 single-molecule trajectories.

III. RESULTS

A. Model-free QENS analysis

For a network-forming liquid such as water, it is convenient and useful to dissect the dynamics into (i) sub-picosecond restricted motions in the intact but distorted network and (ii) slower rearrangements of the network as H-bonds are broken and reformed and molecules exchange places in the network.[1] We refer to these dynamics as vibrational (V) and structural (S), respectively. The V dynamics include O−H librations and H-bond vibrations, with characteristic times of order 100 fs,[3–6] as well as longer-wavelength collective modes.[67,68] (Intramolecular vibrations do not contribute significantly to QENS.) Below room temperature and in the quasielastic energy transfer range, the shape of the

QENS spectrum, $I(Q, \omega)$, is fully determined by the slower S dynamics, while the fast V dynamics only contribute an overall scaling factor and a uniform background, both of which depend on Q but not on ω. Here, the quasielastic regime is taken to extend out to $|\hbar\omega| = 2.5$ meV, corresponding to 0.26 ps.

The QENS spectrum, $I(Q, \omega)$, is a convolution of the dynamic structure factor (DSF), $S(Q, \omega)$, which contains the desired information about S dynamics, and an instrumental resolution function, which in our case can be approximated by a Gaussian (Fig. 1). On general theoretical grounds,[69] we expect that the DSF can be expressed as a weighted sum of Lorentzians. Although, in principle, an infinite number of Lorentzian terms may be involved, we find that only two Lorentzians are needed to accurately fit all our QENS spectra in the investigated ranges of momentum transfer, $0.15 \leq Q \leq 2.15$ Å^{-1}, and temperature, $253 \leq T \leq 293$ K. The two Lorentzians are readily separable since they differ in width by a factor 3–5 (at high Q) or more. The width, $\Gamma_1(Q)$, of the narrow Lorentzian is highly robust, with little or no change when we include a third Lorentzian or when we alter the energy transfer window used for the fit. In contrast, the width, $\Gamma_2(Q)$, of the broad Lorentzian is significantly affected by such modifications. To characterize the broad component accurately, it would probably be necessary to model the V dynamics explicitly.[70] However, in the present model-free analysis, we shall focus on the slower S component probed by $\Gamma_1(Q)$.

The QENS data were thus analyzed with the model-free fitting function in Eq. (2.4). At each Q value, the five parameters in this function were determined from a fit to the QENS spectrum. To determine Γ_1 with good accuracy at small Q and low temperature (where Γ_1 is small), we increased the incident neutron wavelength, λ_0, from 5 to 8 or 12 Å, thus trading lower neutron flux for better energy resolution (Fig. 2). Typical spectral fits are shown in Fig. 3. Importantly, at this stage of the analysis, we do not impose any conditions on the functional form of the Q-dependencies of the fitting parameters. We thus avoid the bias that comes from constraining the functional form of these Q-dependencies (or lack thereof) on the basis of a detailed model that relies on approximations of uncertain validity.

At small Q, we expect the DSF to be a single Lorentzian.[27–29] The relative amplitude, $A(Q)$, of the narrow Lorentzian, which may be regarded as the EISF associated with the dynamics responsible for the broad Lorentzian, does indeed approach unity as $Q \rightarrow 0$ and it shows little or no temperature dependence in the range 253–293 K (Fig. 4). The weak, nearly linear Q-dependence of the EISF in Fig. 4 contrasts with the much stronger Q-dependence, $A(Q) = [j_0(Q b)]^2$ with $b = 0.98$ Å the O−H bond length, that follows from the assumption of rotation–translation decoupling in the standard model.[35,51] Much better agreement, albeit with a somewhat too strong Q-dependence, is obtained with the EISF for a uniformly occupied sphere,[28] $A(Q) = [3 j_1(Q a)/(Q a)]^2$, with the radius, a, identified as the rms radius of gyration, R_{basin}, of the dynamical basin [see Eq. (2.19)], taken as 0.73 Å (the average for the 6 QENS temperatures in Table IV). A virtually identical result is obtained

with a Gaussian confinement model.[71] In the Q range of Fig. 4, the spherical-surface EISF of the standard model can be made to almost coincide with the uniform-sphere EISF provided that b is reduced to 0.56 Å, but then the original geometrical interpretation is lost.

In the quasiharmonic approximation, the scaling factor, $C(Q)$, in Eq. (2.4) can be related to the effective mean-square amplitude, $\langle u^2 \rangle$, of the V dynamics,[27–29]

$$C(Q) = C(0) \exp\left(-\frac{1}{3}\langle u^2 \rangle Q^2\right). \qquad (3.1)$$

If this approximation is valid, a plot of $\ln[C(Q)/C(0)]$ versus Q^2 should be linear. This is indeed the case (Fig. 5) and the rms amplitude, $u_{rms} \equiv \langle u^2 \rangle^{1/2}$, deduced from the slope is $0.56-0.60$ Å, with a weak trend to larger values at higher temperatures (Table III).

The Q-dependent linewidth, $\Gamma_1(Q)$, can be accurately represented by the two-parameter expression,

$$\Gamma_1(Q) = \frac{D Q^2}{1 + (Q d)^2/6}, \qquad (3.2)$$

which has the expected asymptotic ($Q \rightarrow 0$) limit[27–29] and is of the same form as in the standard model.[35] However, in the model to be developed in Sec. III C, the parameter d is not the actual jump length, as in the standard model, but an *apparent* jump length. Figure 6 shows fits of Eq. (3.2) to the linewidths, $\Gamma_1(Q)$, derived from spectral fits like those in Fig. 3 at all six temperatures. Traditionally, such fits are displayed as $\Gamma_1(Q)$ versus Q^2 (Fig. S1),[72] but we prefer to plot $\Gamma_1(Q)/(D Q^2)$ versus Q to reveal data scatter at low Q and to make departures from the asymptotic limit (the horizontal line) more conspicuous and directly comparable between datasets at different temperatures (Fig. 6). The quantity plotted in Fig. 6 may be regarded as an effective, Q-dependent diffusion coefficient, $D_{eff}(Q) \equiv \Gamma_1(Q)/Q^2$, normalized by its $Q \rightarrow 0$ limit, D.

A reduction of $D_{eff}(Q)$ with increasing Q was also found in previous QENS studies, but when $\Gamma_1(Q)$ is determined from a standard-model fit, with $A(Q) = [j_0(Q b)]^2$, this reduction is significantly stronger than the essentially linear reduction that we find for $Q > 1$ Å^{-1} at all temperatures. In Fig. S2,[72] we compare our $\Gamma_1(Q)/(D Q^2)$ results with those reported by Teixeira *et al.*[35] The difference is striking, particularly at lower temperatures and at $Q < 1$ Å (where, unphysically, the older results exceed the asymptotic limit of 1). We attribute these discrepancies to the shortcomings of the standard model and to the lower signal-to-noise and energy resolution in the previous study. Our results in Fig. 6 also deviate from the linewidths obtained from the QENS data measured at higher resolution by Cavatorta *et al.*[36,73] (Fig. S3).[72]

The parameter values deduced from the fits in Fig. 6 are collected in Table III. The macroscopic diffusion coefficient, D, of H_2O has previously been determined in the supercooled regime by pulsed-gradient spin echo NMR (Ref. 53) and, above 273 K, also by tracer techniques.[54] If our QENS analysis is sound, it must produce D values consistent with these more direct measurements. This is indeed the case (Fig. 7, Table III); the average absolute deviation at the six temperatures is merely 1.6%.
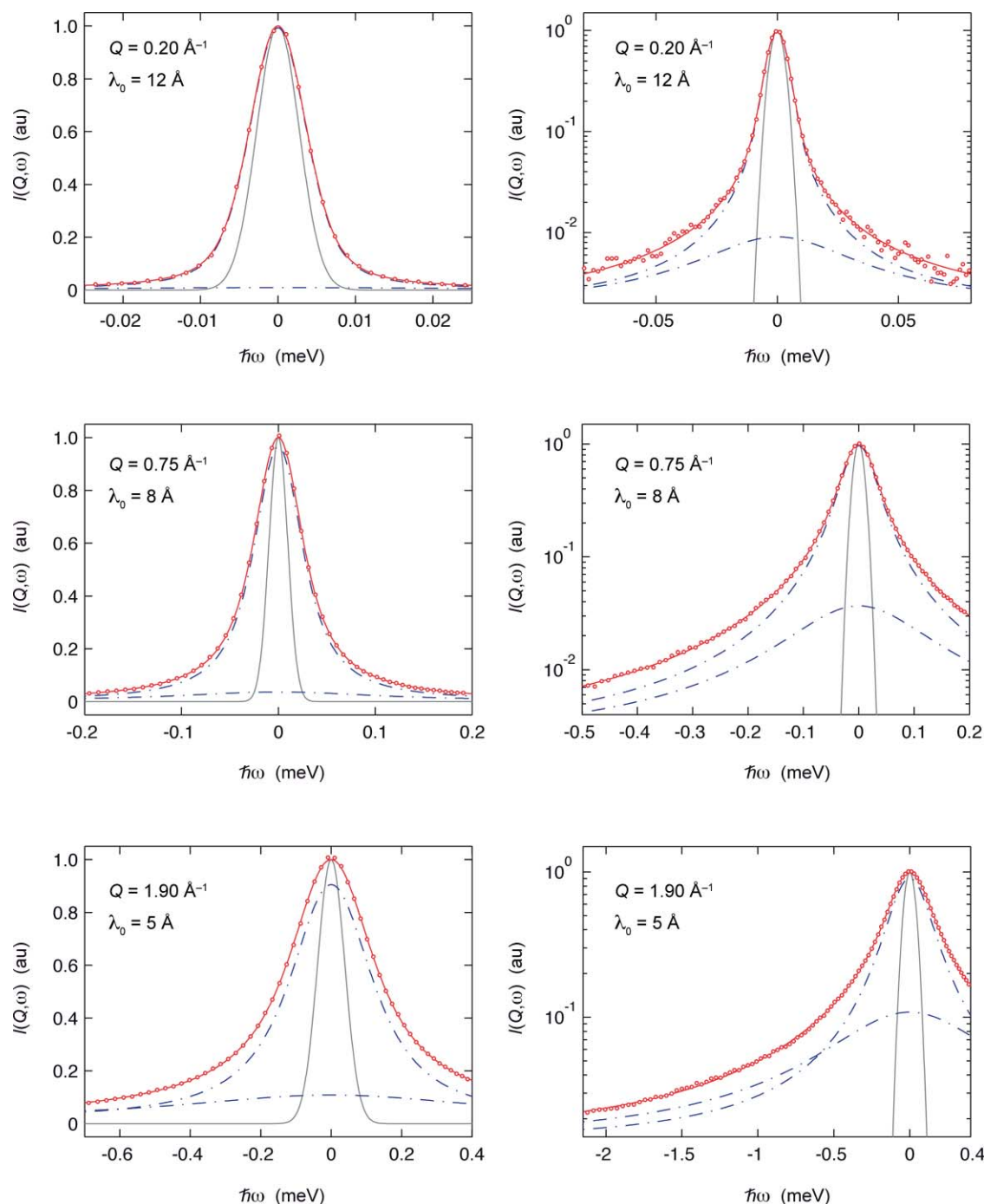
FIG. 3. Normalized QENS spectra from H_2O at 263 K and $Q = 0.20$, 0.75, and 1.90 Å^{-1}, with $\lambda_0 = 12$, 8, and 5 Å, respectively, shown on linear (left) and semilogarithmic (right) scales. The solid curve is a fit according to Eq. (2.4) and the dashed curves are the two Lorentzian components (with the constant background added to each contribution). The gray curve is the resolution function.

B. MD validation of model-free analysis

To support our model-free QENS analysis (Sec. III A), we computed the ISF, $F(Q, \tau)$, from MD simulations with the SPCE water model (Secs. II D and II E) at six temperatures near those used for the QENS experiments (Tables I and II).

Since the SPCE model has been parameterized to reproduce experimental data at ambient conditions,[58] it may produce less accurate results in the supercooled regime. To compensate for such deficiencies, we compare simulation re-

sults with experimental results at an effective temperature, $T_{eff} = T + \Delta T$, rather than at the actual simulation temperature, T, defined by the mean kinetic energy. Noting that the SPCE model yields a temperature of maximum density of 240 K,[74] whereas the experimental value is 277 K,[1] previous authors[22] have used $\Delta T = 37$ K. Since we are concerned here with structural dynamics, which depend very little on density in the temperature range of interest, we use a smaller correction, $\Delta T = 7$ K, which brings the simulated translational diffusion coefficient, D, and ^{17}O rotational correlation time, τ_R,
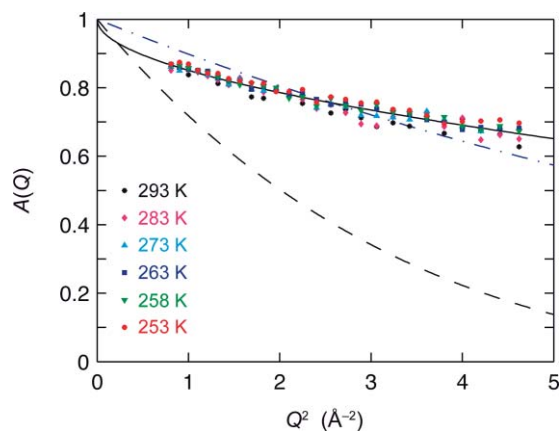
FIG. 4. Q-dependent EISF, obtained from fits as in Fig. 3 at $\lambda_0 = 5$ Å. The solid curve was obtained by fitting the data from all six temperatures to a quadratic polynomial: $A = 1 - 0.1437 Q - 0.0055 Q^2$. The dashed curve is the EISF for a spherical surface of radius 0.98 Å, as in the standard model, and the dashed–dotted curve is the EISF for a uniformly occupied sphere of radius 0.73 Å.

in agreement with the corresponding experimental values in the temperature range 253–293 K (Table II, Sec. II E). For reference, we note that D varies by a factor 4.3 in our 40 K temperature range, whereas the 0.65% density variation[59] within this range corresponds to a mere 2% variation in D (at 277 K).[75] In the following, we refer to the MD simulations by the effective temperature, T_{eff}, given in Table II.

As noted in Sec. III A, we expect V dynamics to be much faster than S dynamics at the investigated temperatures. It should then be possible to choose a time, τ^*, such that the ISF decay for $\tau < \tau^*$ is essentially due to V dynamics, whereas the further decay for $\tau > \tau^*$ is essentially due to S dynamics. The computed ISFs (Figs. 8 and 9), like those reported previously,[22,23,43–45,73] confirm this expectation and suggest $\tau^* = 0.5$ ps, corresponding to $\hbar\omega = 1.3$ meV, as a reasonable
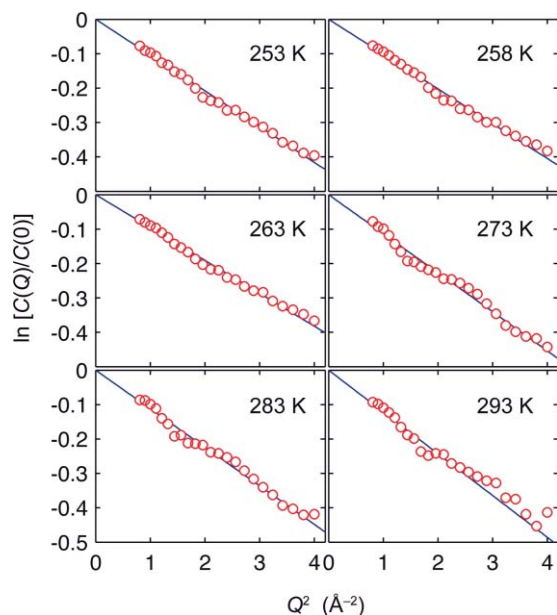

FIG. 5. Debye–Waller plots of the scaling factor $C(Q)$ obtained from fits as in Fig. 3 at $\lambda_0 = 5$ Å.

partition. V and S dynamics can thus be regarded as time scale separated under the conditions of our QENS experiments and the ISF can be decomposed into two independent contributions,

$$F(Q, \tau) = [1 - C^*(Q)] F_V(Q, \tau) + C^*(Q) F_S(Q, \tau),$$

(3.3)

where the Debye–Waller-like factor $C^*(Q)$ can be identified as $F(Q, \tau^*)$ and the partial ISFs $F_V(Q, \tau)$ and $F_S(Q, \tau)$ both decay from 1 to 0. The quantity $C^*(Q)$ differs from the analogous $C(Q)$ in Eqs. (2.4) and (3.1) only by the instrumental factor, $\alpha(\lambda_0)$, introduced in Eq. (2.1).

Fundamentally, QENS probes proton dynamics rather than molecular dynamics. At very small Q this distinction is irrelevant, but at larger Q the interpretation of QENS data in terms of molecular motions is always model dependent. The motion of a proton in the laboratory frame can be formally decomposed into proton motion relative to the molecular COM and COM motion in the laboratory frame. But this decomposition is useful only to the extent that these motional modes are statistically independent (such as normal modes). MD simulations indicate that this is not so.[42,43] The effect of molecular rotation (as defined by the proton–COM vector) on QENS data may be gauged by comparing the proton ISF with the (experimentally inaccessible) ISF for the molecular COM. As noted previously,[42,43] whereas the proton and COM ISFs differ for $\tau < \tau^*$ (primarily because the COM ISF is insensitive to librations), they are nearly identical for $\tau > \tau^*$ apart from a scaling (Fig. 10). At $Q = 2.23$ Å^{-1}, $F_H(Q, \tau^*)/F_{COM}(Q, \tau^*) = 0.964$ and at smaller Q this scaling factor approaches 1. The striking near-superposition of the scaled ISFs for $\tau > \tau^*$, which holds at all investigated temperatures (Fig. S4) (Ref. 72) and Q values, has been attributed to the cancellation of the small rotational contribution to the proton ISF by a rotation–translation cross-term of opposite sign.[43] In practice, it is therefore not possible to extract information about water rotation from QENS data.

The structural ISF is clearly not exponential, but for $\tau > \tau^*$ it can be accurately represented by a weighted sum of two exponentials as in Eq. (2.15) (Fig. 11), supporting our model-free analysis of QENS spectra in terms of two Lorentzians (Sec. III A). Fits of comparable (or somewhat lower) quality are obtained with a stretched exponential ISF, but we prefer the biexponential function since it can be rationalized in terms of microscopic dynamics (Sec. III C).

Interpreting the prefactor, $C^*(Q)$, in Eq. (2.15) according to Eq. (3.1), we obtain from the Debye–Waller plots (Fig. S5) (Ref. 72) rms V amplitudes, u_{rms}, in the range 0.54–0.57 Å at the six temperatures. These MD-derived values are very similar to the u_{rms} values (Table III) deduced from the model-free analysis of our QENS spectra. Considering that intramolecular flexibility and quantum effects are not explicitly accounted for in our simulations, this agreement may well be partly fortuitous.

The relative amplitude, $A(Q)$, of the slowly decaying component of the structural ISF (corresponding to the narrow Lorentzian component of the DSF), obtained by fitting Eq. (2.15) to the MD-derived ISF (Fig. 11), has a similarly weak
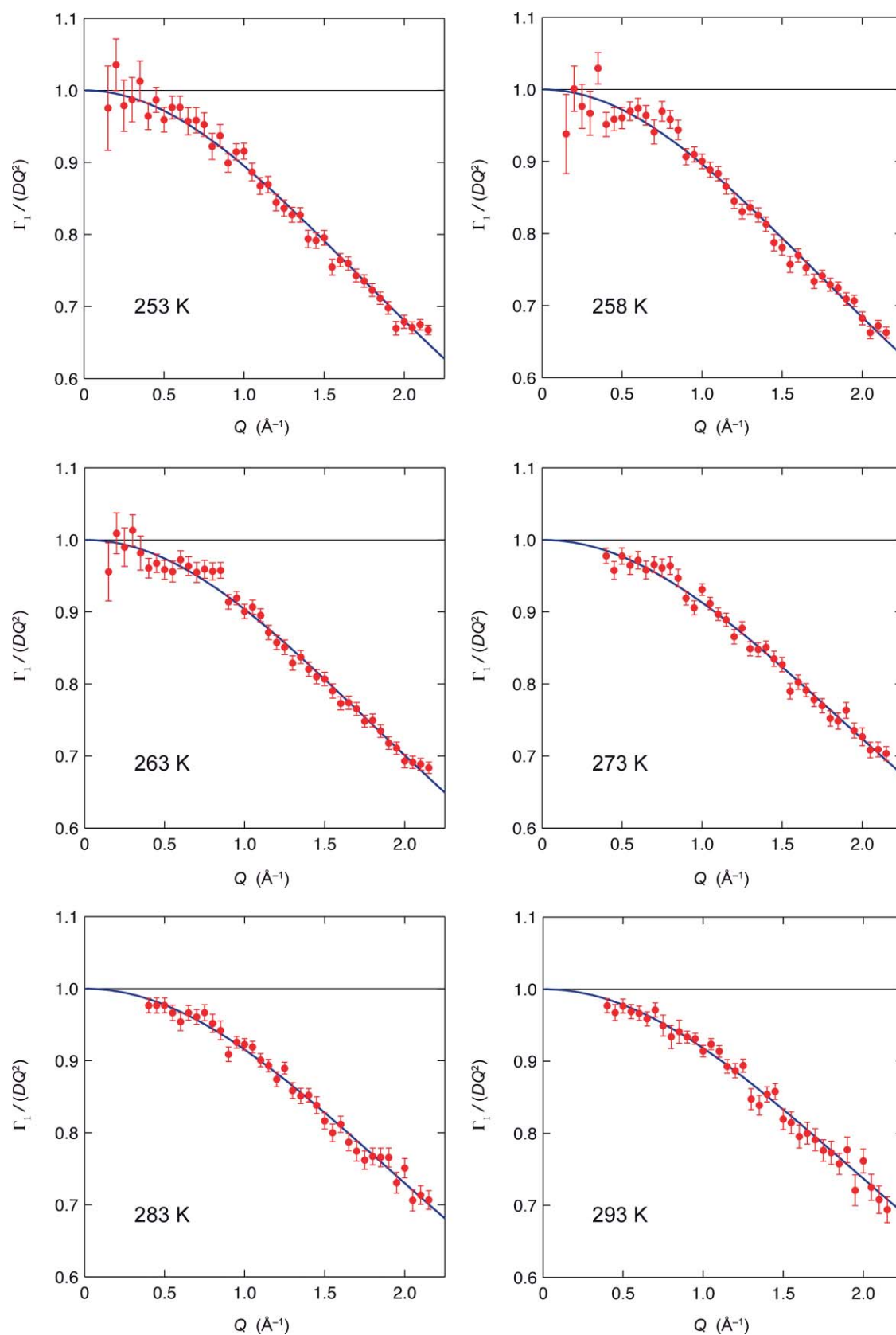
FIG. 6. Q-dependent width of the narrow Lorentzian obtained from fits as in Fig. 3 to spectra recorded at at $\lambda_0 = 5$, 8, or 12 Å and displayed as the effective diffusion coefficient, $\Gamma_1(Q)/Q^2$, normalized by the macroscopic diffusion coefficient, D, deduced from the fit. The solid curve resulted from a fit according to Eq. (3.2) and the horizontal line is the $Q \to 0$ asymptote.
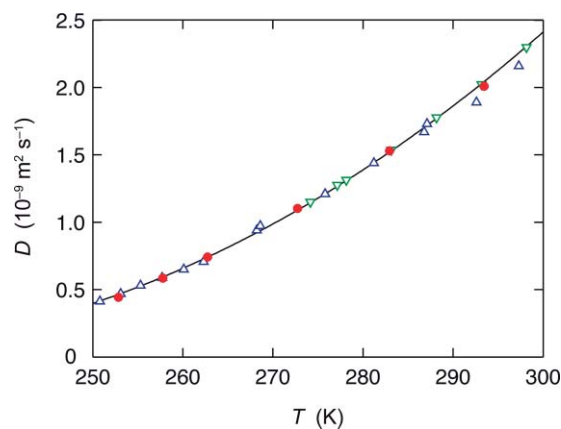
FIG. 7. Temperature-dependent diffusion coefficient of H_2O, obtained from the fits in Fig. 6 (filled red circles), from NMR PGSE measurements (Ref. 53) (blue up-triangles), and from tracer measurements (Ref. 54) (green down-triangles). The curve is the power-law fit in Eq. (2.8).
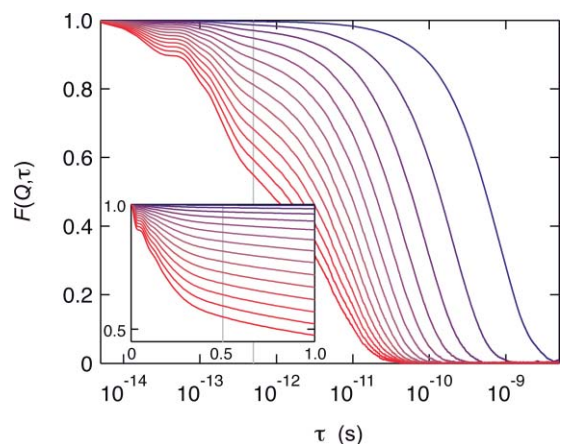

FIG. 8. MD-derived ISF for water protons at 254 K and $Q = n\, Q_{\min}$ with $Q_{\min} = 0.1590$ Å^{-1} and $n = 1 - 14$ (Q decreases from left to right). The inset shows the initial decay on a linear scale (in ps). The vertical gray line is at $\tau^* = 0.5$ ps.

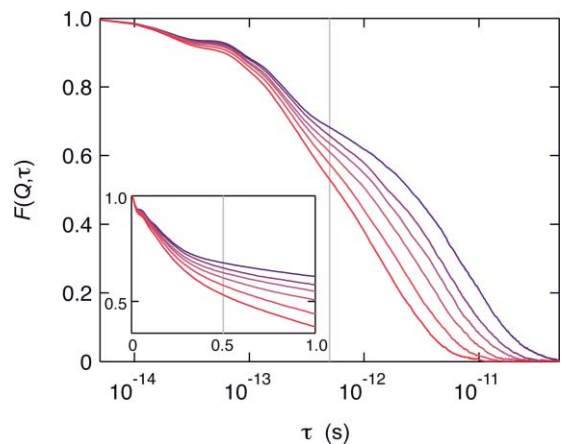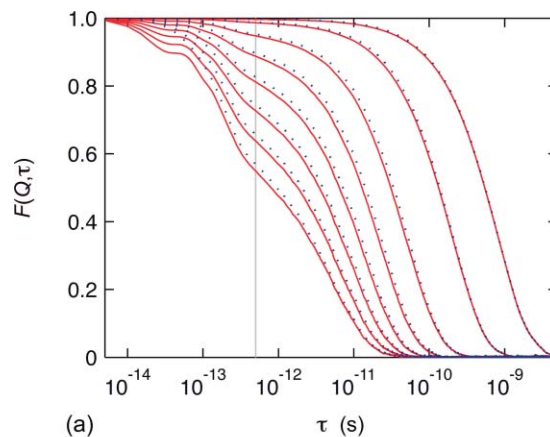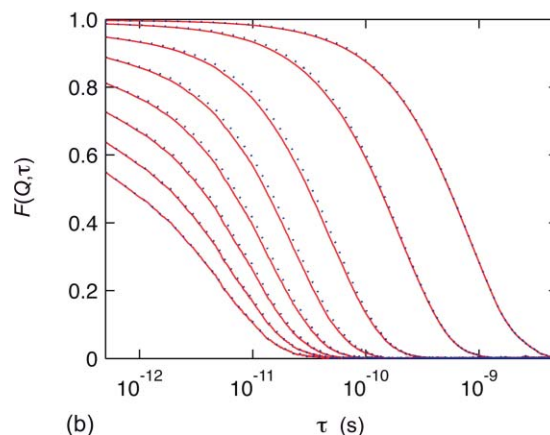FIG. 9. MD-derived ISF for water protons at $Q = 1.75$ Å^{-1} and $T = 254$–297 K (Table II) with T decreasing from left to right. The inset shows the initial decay on a linear scale (in ps). The vertical gray line is at $\tau^* = 0.5$ ps.

FIG. 10. (a) MD-derived ISF for water protons (solid) and molecular COM (dotted) at 254 K and $Q = n\, Q_{\min}$ with $Q_{\min} = 0.1590$ Å^{-1} and $n = 1, 2, 4, \ldots, 14$ (Q decreases from left to right). The vertical gray line is at $\tau^* = 0.5$ ps. (b) The same ISFs as in (a) after scaling so that the proton and COM ISFs coincide at $\tau^* = 0.5$ ps.

Q-dependence (Fig. S6) (Ref. 72) as the $A(Q)$ parameter deduced from the model-free QENS analysis (Fig. 4). Like the latter, it deviates markedly from the Q-dependence prescribed by the standard model.[35,51]
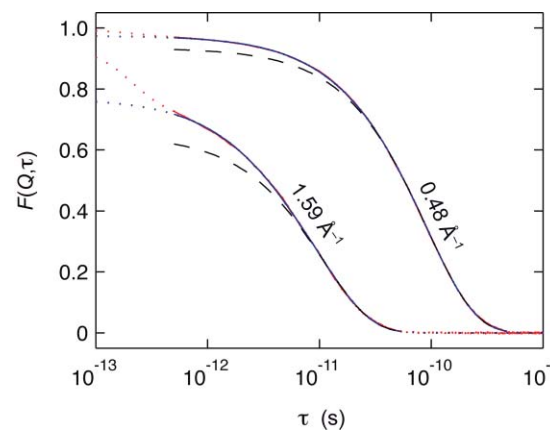

FIG. 11. MD-derived ISFs at 254 K and indicated Q values (red) and biexponential fits (blue) according to Eq. (2.15). The curves are dotted outside the fitting range. The dashed curves show the dominant, slowly decaying, component.

The long decay time, $\tau_1(Q)$, deduced from fits of Eq. (2.15) to the MD-derived ISF corresponds to the inverse of the linewidth, $\Gamma_1(Q)$, of the narrow DSF component. We thus expect the Q-dependence of $1/\tau_1(Q)$ to be described by Eq. (3.2). This is indeed the case (Fig. S7) (Ref. 72) and the effective diffusion coefficient decreases roughly linearly for $Q > 1$ Å^{-1}, as for the QENS data in Fig. 6 but in contrast to the stronger Q-dependence obtained when $\Gamma_1(Q)$ is extracted with the aid of the standard model (Fig. S2).[72] If our analysis is consistent, the diffusion coefficient obtained from the $1/\tau_1(Q)$ fits should agree with the D value determined from a linear fit to the mean-square displacement obtained from the MD trajectory (but without any correction for the finite size of the simulation box,[62] since this effect is also manifested in the ISF). This is indeed the case; the average absolute deviation at the 6 temperatures is merely 0.95%. Finally, the effective jump length, d, deduced from the $1/\tau_1(Q)$ fits is in the range 0.7–0.9 Å, close to the values deduced from the QENS data (Table III).

The ISF in Eq. (3.3) corresponds to a DSF of the form,

$$S(Q, \omega) = [1 - C^*(Q)]\, S_V(Q, \omega) + C^*(Q)\, S_S(Q, \omega),$$

(3.4)

with the vibrational and structural DSFs given by

$$S_V(Q, \omega) = \frac{1}{\pi} \int_0^\infty d\tau \, \cos(\omega \tau) \, F_V(Q, \tau), \qquad (3.5a)$$

$$S_S(Q, \omega) = \frac{1}{\pi} \int_0^\infty d\tau \, \cos(\omega \tau) \, F_S(Q, \tau). \qquad (3.5b)$$

Comparing Eq. (3.4) with the empirical fit function in Eq. (2.4), we see that the DSF used in the QENS analysis can be identified with $C^*(Q)\, S_S(Q, \omega)$ and that the background parameter, $B(Q)$, can be identified with $[1 - C^*(Q)]\, S_V(Q, 0)$. The MD-derived $S_V(Q, \omega)$ is nearly flat in the quasielastic range (Fig. 12), so that it can be approximated by a constant as in Eq. (2.4). Indeed, Fig. 12 shows that the vibrational contribution falls off by merely 3% out to $|\hbar\omega| \approx 1$ meV. For reference, the QENS spectral fit yields $\Gamma_1 \approx 0.1$ meV and $\Gamma_2 \approx 0.5$ meV under conditions close to those of Fig. 12. Furthermore, $[1 - C^*(Q)]\, S_V(Q, 0)$ increases with Q in much the same way as $B(Q)$ does in the model-free QENS analysis. When examined over a wider energy transfer range, the vibrational DSF exhibits the expected librational peak near 60 meV [Fig. 12 (inset)] and the corresponding vibrational density of states shows a broad peak at 6.5 meV associated with collective vibrations.[76] These features are also evident in our QENS data.

C. Microscopic model

The microscopic origin of the two components in the structural ISF (or DSF) is suggested by a visual inspection of MD trajectories. Figure 13 shows the position of the molecular COM during 75 ps at 254 K. The trajectory exhibits a pronounced clustering with six well-defined dynamical clusters. We shall refer to these clusters as basins, but we emphasize
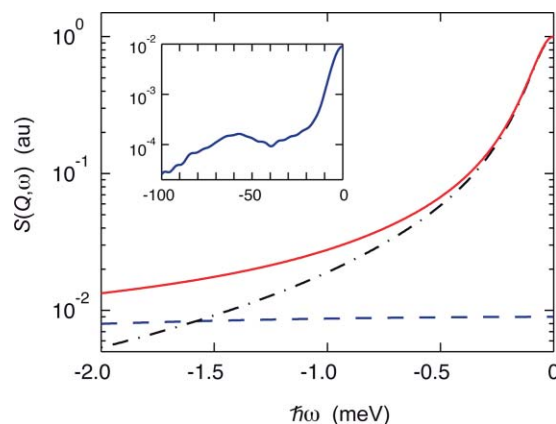

FIG. 12. MD-derived DSF at 260 K and $Q = 1.75$ Å^{-1} (red solid), decomposed into a structural part (black dashed–dotted), $C^*(Q)\, S_S(Q, \omega)$, and a vibrational part (blue dashed), $[1 - C^*(Q)]\, S_V(Q, \omega)$. The latter is shown in the inset over a wide energy transfer range.

that they are not simply related to the basins or metabasins that can be identified from an analysis of the system's potential energy landscape[17,20,21,26] (Sec. IV B). At this temperature, the mean dwell time in a basin is ~10 ps, during which time the molecule undergoes sub-picosecond vibrations as well as local structural fluctuations on a time scale of a few picoseconds. The intrabasin trajectory thus reflects V dynamics as well as the fast component of S dynamics. The transition from one basin to the next is fast compared to the dwell time in a basin so it can be approximated by an instantaneous jump. The slow component in the structural ISF can be identified with these basin-to-basin jumps. At higher temperatures, the basins are less "dense", but the basin picture remains useful throughout the temperature range investigated here. Although QENS probes proton dynamics, the MD analysis presented in the remainder of this section is based on the COM trajectory, which is simpler to analyze (and visualize) since it is not "blurred" by librational oscillations. The intrabasin dynamics of the proton and COM are not identical (although they cannot be distinguished from the ISF beyond $\tau^* \approx 0.5$ ps), but the jump dynamics should be essentially the same for any molecular site.

We thus decompose the structural dynamics into local, intrabasin fluctuations (L), and interbasin jumps (J). The L and J dynamics are assumed to be statistically independent, but not necessarily fully time scale separated. The structural ISF then factorizes as

$$F_S(Q, \tau) = F_L(Q, \tau)\, F_J(Q, \tau). \qquad (3.6)$$

Since the L motions are restricted, $F_L(Q, \tau)$ decays to a finite plateau value, $A(Q)$, often referred to as the elastic incoherent structure factor (EISF).[28] Assuming an exponential decay, we then have

$$F_L(Q, \tau) = A(Q) + [1 - A(Q)]\, \exp\left[-\frac{\tau}{\tau_L(Q)}\right]. \qquad (3.7)$$

Given that the structural ISF can be accurately represented by two exponentials (Fig. 11), a consistent model is obtained by

FIG. 14. Q-dependent intrabasin relaxation time, $\tau_L(Q)$, obtained as $1/(\Gamma_2 - \Gamma_1)$ from QENS fits as in Fig. 3 (filled symbols, at six temperatures) or as $1/(1/\tau_2 - 1/\tau_1)$ from ISF fits as in Fig. 11 (open symbols connected by lines, at 254 and 297 K).
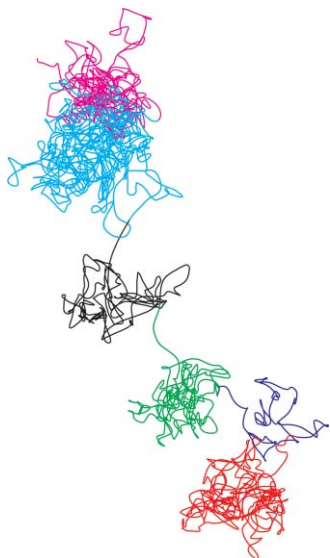

FIG. 13. A 75 ps MD trajectory at 254 K showing the water COM position at 5 fs resolution. The basins, as identified by our coarse-graining algorithm, are color-coded in chronological order: red → 1.51 → blue → 1.86 → green → 2.08 → black → 2.79 → cyan → 1.05 → magenta, where the jump lengths (between basin centers) are given (in Å) between the arrows.

assuming that also $F_J(Q, \tau)$ decays exponentially,

$$F_J(Q, \tau) = \exp\left[-\frac{\tau}{\tau_J(Q)}\right]. \tag{3.8}$$

Combining Eqs. (3.3) and (3.6)–(3.8), Fourier transforming and convoluting with the Gaussian resolution function, we obtain a DSF that is formally identical with the target function, Eq. (2.4), used for the model-free QENS analysis. We can thus identify $\Gamma_1(Q)$ with $1/\tau_J(Q)$ and $\Gamma_2(Q)$ with $1/\tau_L(Q) + 1/\tau_J(Q)$.

Figure 14 shows the intrabasin relaxation time, $\tau_L(Q)$, obtained from QENS spectral fits (Fig. 3) as $1/(\Gamma_2 - \Gamma_1)$ and from fits to the MD-derived ISF (Fig. 11) as $1/(1/\tau_2 - 1/\tau_1)$. The dependence of τ_L on Q is weak, as expected for a spatially restricted motion, and there is good agreement between QENS and MD results, again supporting our analysis. However, τ_L depends to some extent on the choice of energy transfer window for the QENS spectral fit and on the cutoff τ^* for the fit to the structural part of the MD-derived ISF. For example, when τ^* is changed from 0.4 to 0.6 ps, τ_L increases by 36% at 254 K and $Q = 1.11$ Å^{-1}. In contrast, τ_J varies by less than 1%. The temperature dependence of the QENS-derived τ_L is adequately described by the Arrhenius law with a fitted activation energy of 17.2 ± 2.6 kJ mol^{-1} (mean and standard deviation for the 26 Q values in Fig. 14). This value suggests that H-bond rearrangements are involved in L dynamics, albeit to a lesser extent than for the global dynamics, with an effective activation energy of ∼23 kJ mol^{-1} in the same temperature range. [From the power-law representations in Eqs. (2.8) and (2.13), we obtain 22.4 kJ mol^{-1} for D and 24.3 kJ mol^{-1} for τ_R.] Specifically, the significantly lower activation for τ_L than for τ_R supports the conclusion, based on the similarity of the proton and COM ISFs (Fig. 10), that the broad DSF component cannot be attributed to molecul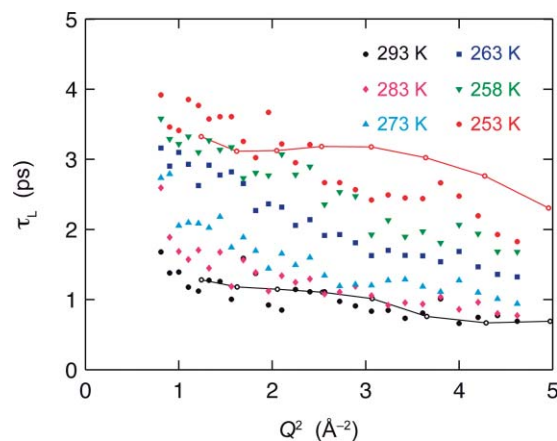ar rotation. In the standard-model analysis, the enforced Q-independent relaxation time associated with this component yielded an activation energy of only 7.7 kJ mol^{-1},[35] which is clearly incompatible with global molecular rotation. Furthermore, in the standard model, this relaxation time should be approximately $3\tau_R$, which is (see Table II) an order of magnitude larger than τ_L in Fig. 14.

To account for the observed Q-dependence in $\tau_J(Q)$ and to interpret the d parameter in Eq. (3.2) we propose to model the slow (J) structural dynamics as a continuous-time random walk (CTRW). The CTRW model was developed in a formal mathematical context by Montroll and Weiss,[77] but it was applied already in Torrey's seminal work on intermolecular dipolar spin relaxation.[78] The CTRW model features both spatial and temporal randomness. The jump vectors, $\boldsymbol{\rho}_i$, are uncorrelated and drawn from the same isotropic distribution, $\varphi(\boldsymbol{\rho})$. Similarly, the time intervals between consecutive jumps, τ_i', are uncorrelated and drawn from the same waiting time distribution, $\psi(\tau')$. The ISF can then be expressed as

$$F_J(Q, \tau) = \sum_{k=0}^{\infty} [\lambda(Q)]^k P_k(\tau), \tag{3.9}$$

where $P_k(\tau)$ is the probability that precisely k jumps occur during an arbitrary time interval τ and $\lambda(Q)$ is the Fourier transform of the jump length distribution,

$$\lambda(Q) \equiv \int d\boldsymbol{\rho} \, \cos(\boldsymbol{Q} \cdot \boldsymbol{\rho}) \, \varphi(\boldsymbol{\rho}). \tag{3.10}$$

In general, the ISF in Eq. (3.9) does not decay exponentially. However, both the QENS and the MD data indicate that, in the investigated temperature range, the jump ISF can be approximated by a single exponential, as in Eq. (3.8). The decay time is then given by

$$\tau_J(Q) = \int_0^{\infty} d\tau \, F_J(Q, \tau). \tag{3.11}$$

Inserting the ISF from Eq. (3.9) into Eq. (3.11) while noting that

$$\int_0^{\infty} d\tau \, P_k(\tau) = \begin{cases} \tau_p, & k = 0, \\ \tau_w, & k \geq 1, \end{cases} \tag{3.12}$$

and summing the resulting geometric series, one obtains[79]

$$\tau_{\mathrm{J}}(Q) = \tau_{\mathrm{p}} + \frac{\lambda(Q)}{1 - \lambda(Q)} \, \tau_{\mathrm{w}}. \tag{3.13}$$

In Eq. (3.12), we introduced the mean waiting time, τ_{w}, and the mean persistence time, τ_{p}, which may be defined in terms of the first and second moments of the waiting time distribution,

$$\tau_{\mathrm{w}} \equiv \int_0^\infty d\tau' \, \tau' \, \psi(\tau'), \tag{3.14a}$$

$$\tau_{\mathrm{p}} \equiv \frac{1}{2\,\tau_{\mathrm{w}}} \int_0^\infty d\tau' \, \tau'^2 \, \psi(\tau'). \tag{3.14b}$$

In the following, we refer to these quantities simply as the waiting time and the persistence time. Whereas τ_{w} is the average time interval between two consecutive jumps, τ_{p} is the average duration from an arbitrary initial time (not necessarily coinciding with a jump) to the next jump. Equation (3.13) shows that the ISF decay time, $\tau_{\mathrm{J}}(Q)$, reports on τ_{p} on small length scales, since $\lambda(Q \to \infty) = 0$, and on τ_{w} on large length scales, since $1 - \lambda(Q \to 0) \sim Q^2$.

To complete the model, we must specify the jump vector distribution, $\varphi(\boldsymbol{\rho})$. But if the jump length is sufficiently small, we can expand the cosine function in Eq. (3.10) to fourth order in $Q\rho$, obtaining

$$\lambda(Q) = 1 - D\,Q^2\,\tau_{\mathrm{w}} + \mu\,(D\,Q^2\,\tau_{\mathrm{w}})^2, \tag{3.15}$$

where we have introduced the macroscopic diffusion coefficient,

$$D \equiv \lim_{\omega \to 0} \lim_{Q \to 0} \frac{\omega^2}{Q^2} \, S_{\mathrm{J}}(Q, \omega) = \frac{\langle \rho^2 \rangle}{6\,\tau_{\mathrm{w}}}, \tag{3.16}$$

and the jump length distribution parameter [related to the kurtosis of $\varphi(\boldsymbol{\rho})$],

$$\mu \equiv \frac{3\,\langle \rho^4 \rangle}{10\,\langle \rho^2 \rangle^2}. \tag{3.17}$$

For a Gaussian distribution, $\mu = 1/2$. If the rms jump length, $\rho_{\mathrm{rms}} \equiv \langle \rho^2 \rangle^{1/2}$, and/or Q is sufficiently small that $Q\,\rho_{\mathrm{rms}} < 3$, the truncation of the $\lambda(Q)$ expansion in Eq. (3.15) introduces an error in $\Gamma_1(Q)$ (see below) of at most 10% (Fig. S8).[72]

Combination of Eqs. (3.13) and (3.15) now yields

$$\tau_{\mathrm{J}}(Q) = \frac{1}{D\,Q^2} + \tau_{\mathrm{w}}\,(\mu + \delta), \tag{3.18}$$

or

$$\Gamma_1(Q) \equiv \frac{1}{\tau_{\mathrm{J}}(Q)} = \frac{D\,Q^2}{1 + (Q d)^2/6}, \tag{3.19}$$

where we have used Eq. (3.16) again and introduced the apparent jump length,

$$d \equiv \rho_{\mathrm{rms}}\,(\mu + \delta)^{1/2}, \tag{3.20}$$

and the dynamical heterogeneity parameter (see below),

$$\delta \equiv \frac{\tau_{\mathrm{p}}}{\tau_{\mathrm{w}}} - 1 = \frac{\langle \tau'^2 \rangle}{2\langle \tau' \rangle^2} - 1. \tag{3.21}$$

In the CTRW model, the jump probability per unit time or jump rate, κ, is not necessarily the same for every jump. However, since the CTRW model is Markovian, it can only describe such dynamical heterogeneity in the limit of annealed disorder, where the jump rates of successive steps are uncorrelated. In the special case of uniform jump rate, that is, in the absence of dynamical heterogeneity, the waiting time distribution is exponential

$$\psi(\tau') = \frac{1}{\tau_{\mathrm{w}}} \, \exp\left(-\frac{\tau'}{\tau_{\mathrm{w}}}\right), \tag{3.22}$$

Equation (3.14) then implies that $\tau_{\mathrm{p}} = \tau_{\mathrm{w}}$ and Eq. (3.21) yields $\delta = 0$, explaining why we call δ the dynamical heterogeneity parameter.

If the waiting time distribution is exponential, the probability $P_k(\tau)$ is given by the Poisson distribution[78,80]

$$P_k(\tau) = \frac{1}{k!} \, \left(\frac{\tau}{\tau_{\mathrm{w}}}\right)^k \exp\left(-\frac{\tau}{\tau_{\mathrm{w}}}\right). \tag{3.23}$$

Substituting this expression into Eq. (3.9) and performing the sum, one finds that the ISF $F_{\mathrm{J}}(Q, \tau)$ decays exponentially, as in Eq. (3.8), with the decay time given by

$$\tau_{\mathrm{J}}(Q) = \frac{\tau_{\mathrm{w}}}{1 - \lambda(Q)}. \tag{3.24}$$

This well-known[33,80] result also follows from Eq. (3.13) by setting $\tau_{\mathrm{p}} = \tau_{\mathrm{w}}$.

Equation (3.19) is identical with the target function, Eq. (3.2), used to fit the observed Q-dependence of the linewidth $\Gamma_1(Q)$ in Fig. 6. The CTRW model thus provides a microscopic rationale for this Q-dependence. Furthermore, by means of Eqs. (3.17), (3.20), and (3.21), we can now link the phenomenological d parameter to the jump length and waiting time distributions via the model parameters ρ_{rms}, μ, and δ. Notably, this connection to microscopic structure and dynamics is general in the sense of not being limited to particular forms of these distribution functions.

D. MD validation of CTRW model

The microscopic model outlined in Sec. III C was inspired by the qualitative appearance of MD trajectories (Fig. 13). We shall now use the simulations to quantitatively validate the CTRW model of the slow structural dynamics and to rationalize the magnitude and temperature dependence of the apparent jump length, d, deduced from the QENS spectra.

Dynamical clustering is an inherent property of the Newtonian MD trajectory. We have devised a simple coarse-graining algorithm (Sec. II F) that successfully identifies the dynamical basins, as illustrated by the color coding in Fig. 13. This projection or mapping of the Newtonian trajectory on a CTRW trajectory produces time series of basin positions and absolute jump times, from which we compute the waiting time and jump length distributions, $\psi(\tau')$ and $\varphi(\rho)$.

The jump length distribution, $\varphi(\rho)$, is nearly Gaussian, except at short jump lengths (Fig. 15). The short-ρ truncation reflects the finite length scale associated with topological rearrangements of the H-bond network. In our coarse-graining
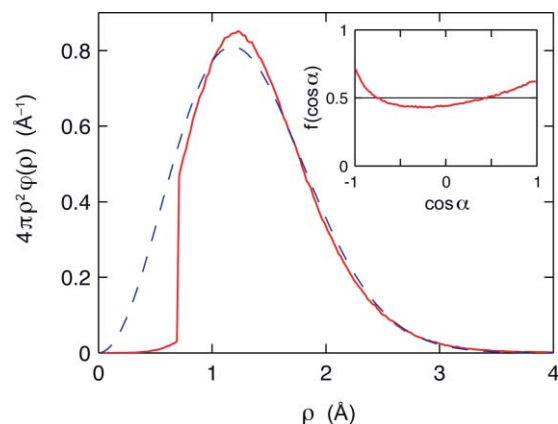
FIG. 15. Jump length distribution (red solid) computed from MD-derived CTRW trajectories at 254 K and Gaussian fit (blue dashed) to data in the 0.7–5 Å interval. The inset shows the distribution of $\cos \alpha$, where α is the angle between successive jump vectors.
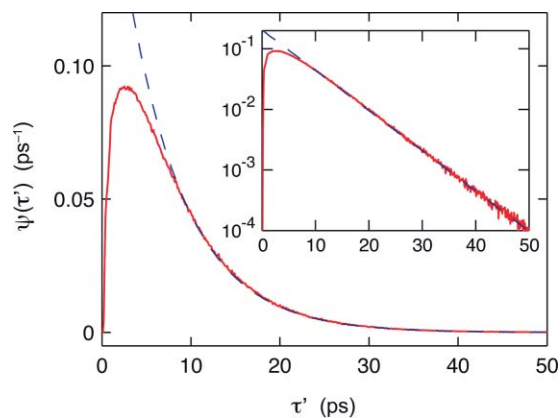

FIG. 16. Waiting time distribution (red solid) computed from MD-derived CTRW trajectories at 254 K and single-exponential fit (blue dashed) to data in the 5–50 ps interval. The inset highlights the exponential character of the distribution on a semilogarithmic scale.

algorithm, this physical feature is implemented by imposing a minimum jump length, $\rho_{\min} = 0.7$ Å (Sec. II F). In other words, two consecutive basins with centers separated by less than $\rho_{\min}$ are not regarded as distinct, but are merged into one basin. (A small nonzero probability remains at $\rho < \rho_{\min}$ because the length of a given jump may decrease below $\rho_{\min}$ when the next two basins are merged.) Computing the second and fourth moments of this distribution, we obtain $\rho_{\rm rms}$ and μ (Table IV). In the contrast to the *apparent* jump length, d, in Table III, the actual rms jump length, $\rho_{\rm rms}$, increases slightly with temperature. The μ parameter is close to 1/2, as expected for a Gaussian distribution.

The inset in Fig. 15 shows the distribution of $\cos \alpha$, where α is the angle between consecutive jump vectors (Sec. II F). The Markovian CTRW model assumes that this distribution is isotropic (horizontal line in Fig. 15) and this is seen to be a good approximation. The average $\langle \cos \alpha \rangle$ is thus close to zero (Table IV), as for an uncorrelated random walk.

The waiting time distribution, $\psi(\tau')$, is exponential at all 6 QENS temperatures, except at short waiting times (Fig. 16). The short-τ' deviation is *not* due to the truncation of the jump length distribution (Fig. 15), but instead reflects a minimum "settling time" before the basin becomes established. This effect becomes relatively more conspicuous at higher temperatures, where the exponential decay of $\psi(\tau')$ occurs on a shorter time scale. As a result of the finite settling time, the dynamical heterogeneity parameter, δ, is slightly negative (Table IV). To rationalize this finding, consider a normalized waiting time distribution of the form $\psi(\tau' < \tau_0) = 0$ and $\psi(\tau' \geq \tau_0) = (1/\hat{\tau}_{\rm w}) \exp[-(\tau' - \tau_0)/\hat{\tau}_{\rm w}]$. For this distribution, Eqs. (3.14) and (3.21) yield a negative δ of $-q\,(1 + q/2)/(1 + q)$ with $q = \tau_0/(2\,\hat{\tau}_{\rm w})$.

The inset in Fig. 16 shows more clearly that the tail of $\psi(\tau')$ does not deviate significantly from exponential form. This is also the case at the higher temperatures indicating that dynamical heterogeneity is *not* an important feature of water translational motion on time scales > 5 ps and at temperatures in the range 254–297 K. However, we cannot exclude the possibility that a modest dynamical heterogeneity (e.g., an underlying biexponentiality) is hidden by the short-τ' settling time effect. A substantial dynamical heterogeneity would be manifested in the DSF as well as in the waiting time distribution.[21] The observed narrow DSF component is very well described by a single Lorentzian (Fig. 3), but a modest dynamical heterogeneity, perhaps caused by a narrow Gaussian distribution of activation energies, might have been difficult to detect via the shape of the QENS spectrum. While neither our QENS data nor our MD simulations provide evidence for dynamical heterogeneity above 253 K, we do find a significant dynamical heterogeneity at lower temperature (Sec. III E).

Using the MD-derived quantities $\rho_{\rm rms}$, μ, and δ in Table IV, we can now calculate the apparent jump length, d, from Eq. (3.20). Although $\rho_{\min}$ was set to 0.7 Å partly to obtain rough agreement with the QENS-derived d values, it is gratifying to note that the MD-derived d values also decrease slightly with increasing temperature (Fig. 17) even though the actual jump length, $\rho_{\rm rms}$, increases (Table IV). The small deviation at the highest temperatures may indicate that the jump description is less applicable there. On increasing $\rho_{\min}$ from 0 to 0.7 Å at 254 K, d increases from 0.82 to 0.86 Å. The $\rho_{\min}$ parameter has virtually no effect on the basin size as gauged by the rms radius, $R_{\rm rms}$, of the trajectory within a basin, which increases slightly with temperature from 0.71 to 0.75 Å (Table IV). The average jump is thus only slightly longer than the average basin diameter, which might explain why the random-walk character of water translation has not been discovered in previous MD simulation studies.

Any discretization of the quasicontinuous MD trajectory, whether it corresponds to dynamical basins or not, will generate an uncorrelated random walk if the sampling of the trajectory is sufficiently coarse. The Einstein–Smoluchowski diffusion coefficient, $D_{\rm ES} = \langle \rho^2 \rangle / (6 \langle \tau \rangle)$, obtained from the coarse-grained trajectory must then agree with the diffusion coefficient, $D_{\rm MSD}$, deduced from the slope of the mean-square displacement for the Newtonian MD trajectory. The coarse-graining algorithm used here, which identifies the dynamical basins, presumably corresponds to the "densest" possible random-walk mapping. Taking into account the small
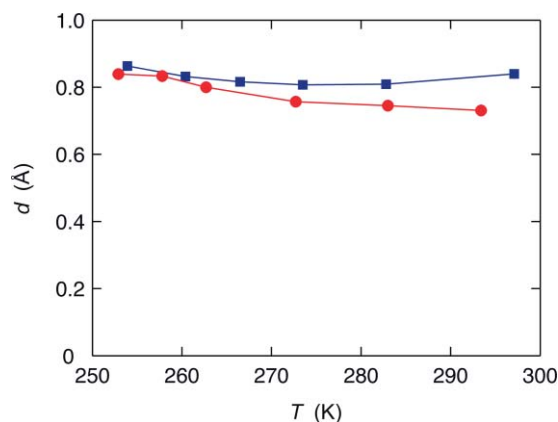
FIG. 17. Apparent jump length, d, derived from analysis of QENS data (red circles) and from MD-derived CTRW trajectories (blue squares). The lines simply connect the data points for visual clarity.

FIG. 18. Jump length distribution (red solid) computed from MD-derived CTRW trajectories at 238 K and Gaussian fit (blue dashed) to data in the 0.7–5 Å interval. The inset shows the distribution of $\cos\alpha$, where α is the angle between successive jump vectors.

residual orientational correlation, as measured by $\langle\cos\alpha\rangle$ (Table IV), we can compute the diffusion coefficient from the CTRW parameters as[81]

$$D_{ES} = \frac{1 + \langle\cos\alpha\rangle}{1 - \langle\cos\alpha\rangle}\frac{\rho_{rms}^2}{6\,\tau_w}. \qquad (3.25)$$

As required, the D_{ES} values thus obtained (Table IV) agree with the corresponding D_{MSD} values at all temperatures (average absolute deviation 0.95%).

Another condition that must be satisfied for D_{ES} to equal D_{MSD} is that the length of a jump must be independent of the time spent in the basin. In other words, jump lengths and waiting times must be statistically independent. It is this assumption in the CTRW model that allows the ISF in Eq. (3.9) to be expressed as a sum of terms that are products of independent spatial and temporal factors. The obtained agreement between D_{ES} and D_{MSD} indicates that the separability approximation is valid. Consistent with this conclusion, direct calculations of the (Pearson) linear correlation coefficient between ρ and τ' yield very small values, ranging from -0.07 at 254 K to -0.03 at 297 K.

E. Dynamical heterogeneity

Whereas our QENS samples did not allow us to reach deeper into the supercooled regime than 252.9 K, MD simulations are, of course, not subject to such limitations. Our philosophy here has been to use simulations to aid the interpretation of QENS data. A systematic exploration of structural dynamics at lower temperatures is therefore beyond the scope of this report. Nevertheless, to justify the generality of the CTRW model and to make predictions for future QENS studies at lower temperatures, we briefly present results from a CTRW analysis of a simulation at $T_{eff} = 237.9$ K (Tables I and II), close to the practical limit of supercooling.[11,12]

The jump length distribution, $\varphi(\rho)$, is now almost perfectly Gaussian above ρ_{min} (Fig. 18). The mean waiting time has more than doubled as compared to 254 K (Table IV) and the $\psi(\tau')$ distribution (Fig. 19) is less influenced by
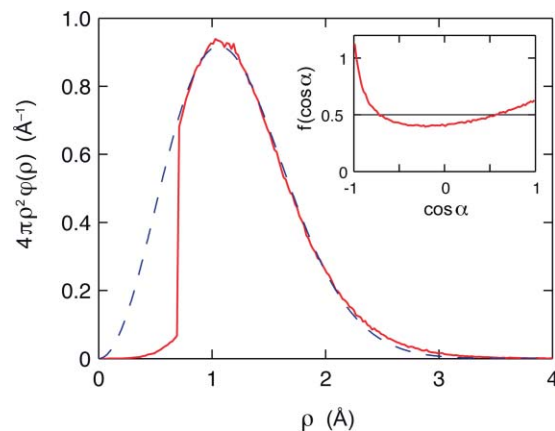
the settling time effect (Sec. III D). Interestingly, the waiting time distribution now deviates significantly from single-exponential form [Fig. 19 (inset)]. A biexponential function provides an excellent fit (Fig. 19) with a minor fast component with $\tau_{wf} = 10.2$ ps and a major (relative weight 0.62) slow component with $\tau_{ws} = 21.0$ ps. The dynamical heterogeneity parameter is now positive, $\delta = 0.05$. The small value of δ at 238 K suggests that there is essentially no dynamical heterogeneity at 254 K (which otherwise could have been masked by the settling time). In principle, dynamical heterogeneity should be manifested in the shape of the narrow component of the QENS spectrum. In practice, the modest dynamical heterogeneity indicated by the 238 K simulation would hardly produce a detectable deviation from Lorentzian shape. Indeed, the MD-derived structural ISF is still well represented by two exponentials (and the fit to a stretched exponential is somewhat worse).

The values of ρ_{rms} and R_{basin} follow the temperature trends established at the higher temperatures (Table IV) and
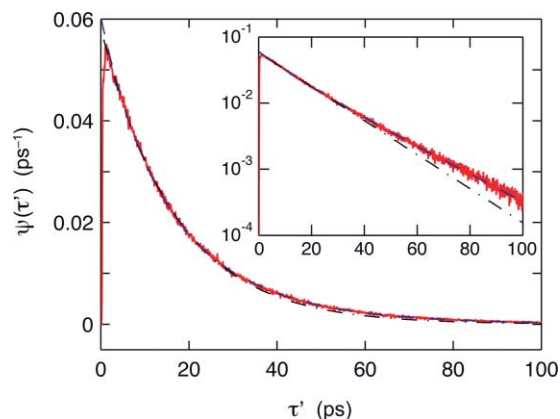

FIG. 19. Waiting time distribution (red solid) computed from MD-derived CTRW trajectories at 238 K, single-exponential fit (black dashed–dotted) to data in the 1.5–25 ps interval, and biexponential fit (blue dashed) to data in the 1.5–100 ps interval. The inset highlights the deviation from single-exponential behavior on a semilogarithmic scale.

the apparent jump length, $d = 1.04$ Å, corresponds to a reduced linewidth of 0.54 at our largest Q value (Fig. 3).

IV. DISCUSSION

A. Continuous diffusion or jumps?

From their seminal MD study of water (at 265 and 308 K) 40 years ago, Rahman and Stillinger concluded that "*the diffusion process proceeds continuously by cooperative interaction of neighbors, rather than through a sequence of discrete hops between positions of temporary residence,*"[82] and subsequent more extensive simulations (down to 206 K) have upheld this view.[22,42] But the MD trajectory in Fig. 13 tells a different story, more in line with the view from the early QENS studies that identified the signature of jumplike motion in the nonclassical Q-dependence of the QENS linewidth.[30,31,34,35] The detailed nature of these inferred jumps has remained elusive.

The picture that emerges from our combined QENS and MD analysis features dynamics on three time scales: vibrational (V) motions, fast local (L) structural dynamics, and slower jumplike (J) structural dynamics. QENS data separate inelastic V motions from quasielastic L+J motions on the basis of their disparate time scales, whereas the MD trajectories (at least in the supercooled regime) separate intrabasin V+L motions from interbasin J motions on the basis of their different spatial extents.

A concise representation of the space-time characteristics of water dynamics is afforded by the MSD, shown in Fig. 20 for the molecular COM at 254 K. The unshaded region in the lower left corner corresponds to V dynamics. This region is bounded by the mean-square vibrational amplitude, $\langle u^2 \rangle = (0.56)^2$ Å^2, which is reached by the MSD at 160 fs. The larger unshaded region in the upper right corner corresponds to J dynamics. This region is bounded by the mean waiting time, $\tau_w = 8.25$ ps, at which time the square root of the MSD has reached 1.8 Å. The linear regime (blue line), where the slope yields D_{MSD}, begins after half a dozen or so jumps. The L dynamics take place in the intermediate shaded region, where the MSD exhibits a plateaulike feature. The rms basin radius, $R_{basin} = 0.71$ Å, the square of which defines the dashed line, is only slightly larger than the rms vibrational amplitude, $u_{rms} = 0.56$ Å.

The long-standing QENS interpretational controversy hinges on the treatment of L and J motions. The standard model[35] misidentifies the L motions as molecular rotation and, in the process, distorts the translational (J) component by enforcing a purely rotational EISF. The standard model identifies the parameter d in Eq. (3.19) with the true rms jump length, ρ_{rms}. As seen from Eq. (3.20), this is correct if $\delta = 0$ *and* if $\mu = 1$. The standard jump model is thus a special case of the more general CTRW model. The condition $\delta = 0$ implies a Poisson process (no dynamical heterogeneity) and the condition $\mu = 1$ implies exponentially distributed jump lengths,

$$\varphi(\boldsymbol{\rho}) = \frac{3}{2\pi\,\rho_{rms}^2\,\rho}\,\exp\left(-\sqrt{6}\,\frac{\rho}{\rho_{rms}}\right). \qquad (4.1)$$
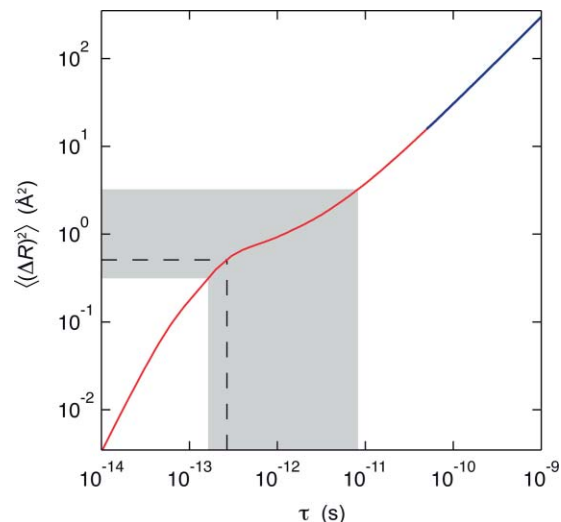

FIG. 20. Mean-square displacement (red) of the molecular COM vs time from the 254 K simulation. The thicker blue part of the curve is the linear regime ($\tau > 50$ ps) used to determine D_{MSD}. The shaded region is bounded from below by the mean-square vibrational amplitude, $\langle u^2 \rangle$, and on the right by the mean waiting time, τ_w. The dashed line corresponds to the mean-square radius of gyration, R_{basin}^2, of dynamical basins.

In contrast, our MD-based CTRW analysis shows that the jump length distribution approximates a Gaussian,

$$\varphi(\boldsymbol{\rho}) = \left(\frac{3}{2\pi\,\rho_{rms}^2}\right)^{3/2}\exp\left(-\frac{3\,\rho^2}{2\,\rho_{rms}^2}\right), \qquad (4.2)$$

for which $\mu = 1/2$. In their pioneering QENS study of supercooled water, Teixeira et al. reported that the rms jump length, ρ_{rms}, *increases* by 85%, from 1.3 to 2.4 Å, on cooling from 293 to 253 K.[35] In contrast, our MD analysis shows that ρ_{rms} *decreases* by 18%, from 1.87 to 1.54 Å, over the same temperature range (Table IV). The main reason for this discrepancy is the spherical-shell EISF, $A(Q) = [j_0(Q\,b)]^2$, imposed by Teixeira et al., which produces a too large and too strongly temperature-dependent deviation of $\Gamma_1(Q)$ from the limiting Q^2-dependence (Fig. S2). Like Teixeira et al., we find that d increases on cooling, albeit less strongly (Table III). Recognizing that d is an apparent jump length that also involves δ (which increases on cooling) and μ, we can reconcile this trend with the opposite (MD-derived) trend in ρ_{rms} (Table IV).

What is the detailed mechanism of the molecular jumps that we identify in the MD trajectories and that are reflected in the QENS data? Our MD analysis is restricted to single-molecule (self) dynamics because this is what is observed by incoherent neutron scattering. But to elucidate the jump mechanism, it is necessary to consider the collective dynamics of the H-bond network. While leaving this task for future work, we make a few remarks here. The CTRW model has considerable generality because it does not make any assumptions about the jump mechanism, details which in any case are not observable by QENS. The class of jump models considered by Chudley and Elliott[33] correspond to the $\delta = 0$ limit of the CTRW model, but since the expansion in Eq. (3.15) was not implemented they presented explicit results only for special choices of the jump length distribution. The picture they had in mind was one of a liquid with "*appreciable short range*

order in a quasicrystalline form" where "*motion takes place in large discrete jumps, between which the atoms oscillate as in a solid.*"[33] This picture features V and J dynamics, but lacks L dynamics. Furthermore, the rms jump length in water at 254 K is 1.5 Å (Table IV), which is only half of the average intermolecular separation. The jump mechanism must, therefore, be considerably more complex than a simple molecular hopping among quasicrystalline lattice positions.

The well-known model introduced by Singwi and Sjölander[32] specifically to describe water dynamics is not really a jump model at all, although it reduces to Eq. (3.19) under certain conditions. The Singwi–Sjölander model (SSM) sets out to describe the water dynamics expected for a particular structural model of liquid water known as the flickering cluster model.[83] According to the latter, liquid water consists of "*cooperatively bonded flickering clusters of ice-like material surrounded by, and alternating roles with, disordered fluid.*"[83] The SSM is a two-state exchange model where a water molecule experiences random transitions between two dynamical states with no mobility (icelike clusters) or with finite mobility (disordered fluid). These transitions represent structural dynamics in the H-bond network, rather than spatial jumps of the reference water molecule. Three assumptions are needed to obtain Eq. (3.19) from the SSM: (*i*) at any time, only a small fraction of the molecules are in the mobile state, (*ii*) water molecules move by *continuous* diffusion in the mobile state, and (*iii*) state exchange is a Poisson process (meaning that the residence times in either state are exponentially distributed). In the SSM, the *d* parameter in Eq. (3.19) is not related to a jump length; it is simply the rms displacement suffered during a visit to the mobile state. And because these displacements are assumed to proceed via continuous diffusion, their distribution is Gaussian, as in Eq. (4.2). Since assumption (*i*) implies that the mean residence time in the mobile state is much shorter than the mean residence time in the immobile state, the continuous displacements can be reinterpreted as jumps. Dynamical heterogeneity, which the SSM ignores, would arise if immobile clusters of different sizes had different transition rates to the mobile state. While the SSM may not be based on an accurate picture of water structure and dynamics, the fact that it predicts the same Q-dependence for $\Gamma_1(Q)$ as does the CTRW model illustrates the limitations of the QENS technique in resolving mechanistic details.

B. On cages, basins, and metabasins

More recent QENS studies of water and aqueous systems tend to favor the RCM,[44–50] where the structural ISF, corresponding to the entire observed QENS spectrum, is fitted with a stretched exponential function,

$$F_S(Q, \tau) = \exp\left[-\frac{\tau}{\tau_K(Q)}\right]^{\beta(Q)}, \qquad (4.3)$$

in place of the biexponential function predicted by our "LJ model" (Sec. III C),

$$F_S(Q, \tau) = \left\{ A(Q) + [1 - A(Q)] \exp\left[-\frac{\tau}{\tau_L(Q)}\right] \right\}$$
$$\times \exp\left[-\frac{\tau}{\tau_J(Q)}\right]. \qquad (4.4)$$

The stretched exponential function is sometimes justified by its ability to fit data with only two adjustable parameters. For the data considered here, the biexponential function provides fits of equal or better quality (as judged by χ^2), albeit with one more parameter. Ultimately, however, the choice of model must be made on the basis of physical argument rather than on fitting capacity.

The MD analysis presented in Sec. III provides strong support for the LJ model, with L and J structural dynamics on distinct length and time scales. The physical significance of the three parameters is transparent, although we have only presented a detailed model for $\tau_J(Q)$. The RCM does not distinguish L and J dynamics; in fact, it does not make explicit reference to jumps at all. The distinct and physically reasonable Q-dependencies in the three parameters of the LJ model contrast with the less transparent Q-dependencies in the 2 RCM parameters. In particular, a stretching exponent, $\beta(Q)$, less than 1, as invariably found by RCM analysis, is interpreted as evidence for heterogeneous structural dynamics. In contrast, our LJ analysis indicates that the dominant J component is dynamically homogeneous in the investigated temperature range. The stretched exponential function successfully describes structural relaxation in many glass-forming liquids close to the glass transition temperature, T_g, where there is strong dynamical heterogeneity.[15,18–20] But the dynamical heterogeneity implied by descriptions of water dynamics with the same function (with $\beta < 1$) may be an artifact of putting two different physical beasts (L and J dynamics) in the same conceptual (α relaxation) and mathematical (stretched exponential) cage.

We initially attempted to analyze the QENS data by assuming, as the RCM does, that there is only one type of structural dynamics and that the apparent two-component shape of the QENS spectrum reflects dynamical heterogeneity. In analogy with Eq. (3.11), we then defined an effective ISF decay time as

$$\tau_S(Q) = \int_0^\infty d\tau \, F_S(Q, \tau). \qquad (4.5)$$

We still used Eq. (2.4) to fit the QENS spectra, but the two Lorentzians were then regarded merely as a convenient numerical representation, without physical significance, that allowed us to deduce the effective decay time as

$$\tau_S(Q) = \frac{A(Q)}{\Gamma_1(Q)} + \frac{1 - A(Q)}{\Gamma_2(Q)}. \qquad (4.6)$$

Two findings led us to abandon this view in favor of the LJ model. First, when the Q-dependence of $\tau_S(Q)$ was analyzed with Eq. (3.2), the resulting diffusion coefficient, D, was found to exceed the value determined more reliably with NMR and tracer techniques[53,54] by about 10% at all temperatures. Second, our MD analysis indicated that structural relaxation, that is, changes in the H-bond network topology as opposed to vibrations within the intact network, occurs both within the dynamical basins and as basin-to-basin jumps. Specifically, the mean waiting time, τ_w (Table IV), in a basin is comparable (within a factor 2) to the rotational correlation time, τ_R (Table II), implying that not only V dynamics but also some S dynamics takes place within the basin.

The RCM draws inspiration and uses terminology from glass physics, in particular mode coupling theory (MCT).[18] The MCT attributes the "plateau" in the MSD (Fig. 20) and in the ISF (Figs. 8–10) to a cage effect, with fast "β fluctuations" within the cage and a slower "α relaxation" associated with the breakup of the cage. This picture is probably appropriate for simple atomic fluids, where repulsive forces are dominant. But it might not capture the more complex structural dynamics in water, where the H-bond network governs structure and dynamics, making the cage metaphor less apt. As one consequence of this additional complexity in water, we believe that it is essential to explicitly recognize the distinct space-time characteristics of L and J dynamics. These distinct characteristics may also rationalize the unusual low-temperature behavior of water[11,12,14] if, as seems likely,[84] the highly collective structural (J) dynamics freeze out at the apparent singularity near 220 K, while the local (L) structural dynamics freeze out at the calorimetric glass transition, $T_g \approx 136$ K.

Important insights about the kinetics and thermodynamics of glass-forming liquids have been obtained by analyzing the topography of the potential energy landscape (PEL), the hypersurface describing the total potential energy of an N-particle system as a function of all particle coordinates.[17,20,21] The PEL can be constructed from an MD trajectory by repeated energy minimizations (quenches). The local energy minima thus obtained are known as inherent structures and the configurations that would be quenched into a particular inherent structure represent a basin (of attraction).[85] Further coarse-graining can be achieved by grouping adjacent basins separated by small barriers into metabasins.[85]

For want of a better term, we refer to the dynamical clusters in the single-molecule trajectory (Fig. 13) as basins. These dynamical basins should not be equated with the energetic basins derived from the PEL. These two types of coarse-graining both achieve the objective of filtering out V dynamics, but they differ in essential ways. An energetic basin is a size-dependent property of the N-particle system, whereas a dynamical basin is a system-size-independent property of the single-particle trajectory. For a system of 216 SPCE water molecules, the mean residence time in a PEL basin is of order $\sim$1 fs even at 180 K,[25] many orders of magnitude shorter than the mean waiting time in a dynamical basin.

For the same system, metabasins were defined as low-mobility regions in the system-averaged MSD and the estimated mean lifetime of a metabasin at 210 K was found to be of the same order of magnitude as the structural relaxation time derived from the decay of the ISF at $Q = 1.8$ Å^{-1} (the first maximum in the static O-atom structure factor).[26] While this apparent link between N-particle PEL and single-particle dynamics is intriguing, several caveats should be borne in mind. First, the system-size dependence of metabasin dynamics is not yet fully understood. Second, the important role of energy–entropy compensation in water is not fully captured by PEL-based metabasin analysis. Third, most simulation studies of supercooled water have focused on temperatures that, according to our "correspondence rule" (Table II, Sec. II A), are well below the experimentally accessible

range. In other words, they explore the region that is sometimes called "no man's land."

The CTRW model has been used to analyze transitions among PEL-derived metabasins in simple model fluids, such as the binary mixture Lennard-Jones system.[21,79] However, such studies typically explore conditions close to the glass transition temperature, T_g, where the dynamical heterogeneity is very strong. For example, one study found a dynamical heterogeneity parameter, $\delta = 26$, and an exponential jump length distribution.[79] In contrast, for water in the experimentally accessible supercooled regime, we find a Gaussian step length distribution and little or no dynamical heterogeneity, with $\delta = 0.05$ at 238 K. This disparity reflects the different physics of repulsion-dominated atomic fluids and network-forming liquids such as water and cautions us against indiscriminate transfer of concepts and theories, such as MCT, from the former to the latter.

[1] D. Eisenberg and W. Kauzmann, *The Structure and Properties of Water* (Clarendon, Oxford, 1969).

[2] G. N. I. Clark, C. D. Cappa, J. D. Smith, R. J. Saykally, and T. Head-Gordon, Mol. Phys. **108**, 1415 (2010).

[3] D. Kraemer, M. L. Cowan, A. Paarmann, N. Huse, E. T. J. Nibbering, T. Elsaesser, and R. J. D. Miller, Proc. Natl. Acad. Sci. U.S.A. **105**, 437 (2008).

[4] S. T. Roberts, K. Ramasesha, and A. Tokmakoff, Acc. Chem. Res. **42**, 1239 (2009).

[5] T. Yagasaki and S. Saito, Acc. Chem. Res. **42**, 1250 (2009).

[6] H. J. Bakker and J. L. Skinner, Chem. Rev. **110**, 1498 (2010).

[7] A. Luzar and D. Chandler, Nature **379**, 55 (1996).

[8] D. Laage and J. T. Hynes, Science **311**, 832 (2006).

[9] G. Stirnemann and D. Laage, J. Phys. Chem. Lett. **1**, 1511 (2010).

[10] I. Ohmine, J. Phys. Chem. **99**, 6767 (1995).

[11] C. A. Angell, Annu. Rev. Phys. Chem. **34**, 593 (1983).

[12] P. G. Debenedetti, J. Phys. Condens. Matter **15**, R1669 (2003).

[13] R. J. Speedy and C. A. Angell, J. Chem. Phys. **65**, 851 (1976).

[14] C. A. Angell, Science **319**, 582 (2008).

[15] C. A. Angell, K. L. Ngai, G. B. McKenna, P. F. McMillan, and S. W. Martin, J. Appl. Phys. **88**, 3113 (2000).

[16] M. Goldstein, J. Chem. Phys. **51**, 3728 (1969).

[17] F. H. Stillinger, Phys. Rev. B **41**, 2409 (1990).

[18] W. Götze and L. Sjögren, Rep. Prog. Phys. **55**, 241 (1992).

[19] P. G. Debenedetti, *Metastable Liquids* (Princeton University, Princeton, NJ, 1996).

[20] P. G. Debenedetti and F. H. Stillinger, Nature **410**, 259 (2001).

[21] A. Heuer, J. Phys. Condens. Matter **20**, 373101 (2008).

[22] F. Sciortino, P. Gallo, P. Tartaglia, and S.-H. Chen, Phys. Rev. E **54**, 6331 (1996).

[23] F. Sciortino, L. Fabbian, S.-H. Chen, and P. Tartaglia, Phys. Rev. E **56**, 5397 (1997).

[24] A. Scala, F. W. Starr, E. L. Nave, F. Sciortino, and H. E. Stanley, Nature **406**, 166 (2000).

[25] N. Giovambattista, F. W. Starr, F. Sciortino, S. V. Buldyrev, and H. E. Stanley, Phys. Rev. E **65**, 041502 (2002).

[26] J. A. Rodríguez Fris, G. A. Appignanesi, E. La Nave, and F. Sciortino, Phys. Rev. E **75**, 041501 (2007).

[27] S. W. Lovesey, *Theory of Neutron Scattering from Condensed Matter* (Clarendon, Oxford, 1984), Vol. 1.

[28] M. Bée, *Quasielastic Neutron Scattering* (Hilger, Bristol, 1988).

[29]P. A. Egelstaff, *An Introduction to the Liquid State*, 2nd ed. (Clarendon, Oxford, 1994).

[30]M. Sakamoto, B. N. Brockhouse, R. G. Johnson, and N. K. Pope, J. Phys. Soc. Jpn. **17** (Suppl. B2), 370 (1962).

[31]P. von Blanckenhagen, Ber. Bunsenges. Phys. Chem. **76**, 891 (1972).

[32]K. S. Singwi and A. Sjölander, Phys. Rev. **119**, 863 (1960).

[33]C. T. Chudley and R. J. Elliott, Proc. Phys. Soc. London **77**, 353 (1961).

[34]S.-H. Chen, J. Teixeira, and R. Nicklow, Phys. Rev. A **26**, 3477 (1982).

[35]J. Teixeira, M.-C. Bellissent-Funel, S.-H. Chen, and A. J. Dianoux, Phys. Rev. A **31**, 1913 (1985).

[36]F. Cavatorta, A. Deriu, D. D. Cola, and H. D. Middendorf, J. Phys. Condens. Matter **6**, A113 (1994).

[37]D. Russo, R. K. Murarka, J. R. D. Copley, and T. Head-Gordon, J. Phys. Chem. B **109**, 12966 (2005).

[38]M. R. Harpham, N. E. Levinger, and B. M. Ladanyi, J. Phys. Chem. B **112**, 283 (2008).

[39]J. Teixeira, M.-C. Bellissent-Funel, and S.-H. Chen, J. Mol. Liq. **48**, 123 (1991).

[40]D. Laage, J. Phys. Chem. B **113**, 2684 (2009).

[41]D. Laage and J. T. Hynes, J. Phys. Chem. B **112**, 14230 (2008).

[42]J. J. Ullo, Phys. Rev. A **36**, 816 (1987).

[43]S.-H. Chen, P. Gallo, F. Sciortino, and P. Tartaglia, Phys. Rev. E **56**, 4231 (1997).

[44]S.-H. Chen, C. Liao, F. Sciortino, P. Gallo, and P. Tartaglia, Phys. Rev. E **59**, 6708 (1999).

[45]L. Liu, A. Faraone, and S.-H. Chen, Phys. Rev. E **65**, 041506 (2002).

[46]A. Cunsolo, A. Orecchini, C. Petrillo, and F. Sacchetti, J. Chem. Phys. **124**, 084503 (2006).

[47]A. Cunsolo, A. Orecchini, C. Petrillo, and F. Sacchetti, J. Phys. Chem. B **114**, 16713 (2010).

[48]L. Liu, A. Faraone, C.-Y. Mou, C.-W. Yen, and S.-H. Chen, J. Phys. Condens. Matter **16**, S5403 (2004).

[49]M. Nakada, K. Maruyama, O. Yamamuro, and M. Misawa, J. Chem. Phys. **130**, 074503 (2009).

[50]E. Mamontov, J. Phys. Chem. B **113**, 14073 (2009).

[51]V. F. Sears, Can. J. Phys. **45**, 237 (1967).

[52]E. Farhi, V. Hugovieux, M. R. Johnson, and W. Kob, J. Comput. Phys. **228**, 5251 (2009).

[53]W. S. Price, H. Ide, and Y. Arata, J. Phys. Chem. A **103**, 448 (1999).

[54]R. Mills, J. Phys. Chem. **77**, 685 (1973).

[55]J. Ollivier and J.-M. Zanotti, Collection SFN **10**, 379 (2010).

[56]J. A. C. Weideman, SIAM (Soc. Ind. Appl. Math.) J. Numer. Anal. **31**, 1497 (1994).

[57]B. Hess, C. Kutzner, D. van der Spoel, and E. Lindahl, J. Chem. Theory Comput. **4**, 435 (2008).

[58]H. J. C. Berendsen, J. R. Grigera, and T. P. Straatsma, J. Phys. Chem. **91**, 6269 (1987).

[59]D. E. Hare and C. M. Sorensen, J. Chem. Phys. **87**, 4840 (1987).

[60]M. P. Allen and D. J. Tildesley, *Computer Simulation of Liquids* (Clarendon, Oxford, 1987).

[61]D. van der Spoel, P. J. van Maaren, and H. J. C. Berendsen, J. Chem. Phys. **108**, 10220 (1998).

[62]I.-C. Yeh and G. Hummer, J. Phys. Chem. B **108**, 15873 (2004).

[63]C. H. Cho, J. Urquidi, S. Singh, and G. W. Robinson, J. Phys. Chem. B **103**, 1991 (1999).

[64]A. Abragam, *The Principles of Nuclear Magnetism* (Clarendon, Oxford, 1961).

[65]J. C. Hindman, J. Chem. Phys. **60**, 4488 (1974).

[66]R. Ludwig, F. Weinhold, and T. C. Farrar, J. Chem. Phys. **103**, 6941 (1995).

[67]G. Ruocco and F. Sette, Condens. Matter Phys. **11**, 29 (2008).

[68]A. Cimatoribus, S. Saccani, F. Bencivenga, A. Gessini, M. G. Izzo, and C. Masciovecchio, New J. Phys. **12**, 053008 (2010).

[69]N. G. van Kampen, *Stochastic Processes in Physics and Chemistry* (North-Holland, Amsterdam, 1981).

[70]H. Schober, Collection SFN **10**, 159 (2010).

[71]F. Volino, J.-C. Perrin, and S. Lyonnard, J. Phys. Chem. B **110**, 11217 (2006).

[72]See supplementary material at http://dx.doi.org/10.1063/1.3578472 for supporting figures S1– S8.

[73]D. D. Cola, A. Deriu, M. Sampoli, and A. Torcini, J. Chem. Phys. **104**, 4223 (1996).

[74]T. Bryk and A. D. J. Haymet, Mol. Simul. **30**, 131 (2004).

[75]K. R. Harris and L. A. Woolf, J. Chem. Soc., Faraday Trans. **176**, 377 (1980).

[76]M.-C. Bellissent-Funel and J. Teixeira, J. Mol. Struct. **250**, 213 (1991).

[77]E. W. Montroll and G. H. Weiss, J. Math. Phys. **6**, 167 (1965).

[78]H. C. Torrey, Phys. Rev. **92**, 962 (1953).

[79]O. Rubner and A. Heuer, Phys. Rev. E **78**, 011504 (2008).

[80]P. L. Hall and D. K. Ross, Mol. Phys. **42**, 673 (1981).

[81]J. W. Haus and K. W. Kehr, Phys. Rep. **150**, 263 (1987).

[82]A. Rahman and F. H. Stillinger, J. Chem. Phys. **55**, 3336 (1971).

[83]H. S. Frank, Proc. R. Soc. London, Ser. A **247**, 481 (1958).

[84]J. Swenson and J. Teixeira, J. Chem. Phys. **132**, 014508 (2010).

[85]F. H. Stillinger and T. A. Weber, Phys. Rev. A **25**, 978 (1982).